Occurrence rates and variability of whistler-mode waves in the plasma trough

C. E. J. Watt[1], N. P. Meredith[2], J. Wong[2,3], K. R. Murphy[1,4], I. J. Rae[1], S. Chakraborty[1], S. N. Bentley[1], O. Allanson[5,6,7], C. J. Rodger[8]

[1]Department of Mathematics, Physics and Electrical Engineering, Northumbria University, Newcastle upon Tyne, UK
[2]British Antarctic Survey, Cambridge, UK
[3]European Centre for Medium Range Weather Forecasts, Reading, UK
[4]Physics, Lakehead University, Thunder Bay, Canada
[5]Space Environment and Radio Engineering, Electronic, Electrical and Systems Engineering, School of Engineering, University of Birmingham, Birmingham, UK
[6]Environmental Mathematics, Department of Earth and Environmental Sciences, University of Exeter, Penryn, UK
[7]Department of Mathematics, Department of Earth and Environmental Sciences, University of Exeter, Exeter, UK
[8]Department of Physics, University of Otago, Dunedin, New Zealand

Key Points:

- Whistler-mode wave variability over short time scales can separate substorm-driven chorus from exohiss despite overlap in frequency
- Chorus and exohiss have different occurrence rates, spatio-temporal behavior and response to driving factors
- Using our analysis, diffusion coefficient models could be reformulated to avoid averaging over two different types of wave activity

Corresponding author: Clare Watt, clare.watt@northumbria.ac.uk

Abstract

Numerical models of energetic electron behavior in the outer radiation belt require descriptions of the wave-particle interactions across the inner magnetosphere. Quasilinear diffusion coefficients describe gyro-resonant wave-particle interactions over large time- and length-scales but these must be constrained by observations to construct realistic radiation belt models. Recent work indicates the importance of identifying and including realistic spatio-temporal variation of diffusion coefficients. In this paper, we study the spatio-temporal variability of whistler-mode waves outside the plasmasphere, typically referred to as whistler-mode chorus. We separately consider the probability of (i) parts of the model domain being outside the plasmasphere, and (ii) the probability of detecting wave activity should that part of the model domain be outside the plasmasphere. We discover that the spatio-temporal variability of whistler-mode waves significantly differs across the model domain; we propose that wave power variability in short wave intervals ($\sim$ 5 minutes) is a useful characteristic to distinguish between two types of whistler-mode waves, especially where their frequency ranges overlap. Our novel spatio-temporal variability analysis indicates that low variability waves are dayside exohiss whose typically high occurrence rate (~ 0.8) decreases with substorm activity, and high variability waves are sporadic post-midnight/dawn sector substorm-driven chorus with a typical occurrence rate of 0.2. Further, although previous studies often combine the occurrence rates and wave characteristics into climatological averages of chorus wave power, this study highlights the importance of separating the study of occurrence rates and power of the waves, since each can have a different relationship with driving factors.

Plain Language Summary

Naturally-occurring electromagnetic waves with frequencies in the range of a hundred to a few thousand Hertz interact with the high-energy electrons of the radiation belt. The resulting wave-particle interactions lead to both energisation and scattering of high-energy electrons, influencing the number and energy of electrons trapped in Earth's outer radiation belt. Wave-particle interactions can be captured using diffusion coefficients that describe the efficacy of the interaction. Our main challenge when building models of diffusion coefficients is to model how they vary in time and throughout near-Earth space, even though we have only very sparse spacecraft observations to help build up our knowledge. The new results in this paper use a statistical analysis of wave activity measured by the NASA Van Allen Probes to determine the spatio-temporal variation of electromagnetic waves known as whistler-mode chorus. We study how the occurrence rate of these waves varies in space, and in response to geomagnetic activity. We also demonstrate that waves in different regions of space display variability on short timescales. The short timescale variability can be used to distinguish one type of waves from another, allowing us to model their occurrence and behavior more accurately in future.

1 Introduction

Wave-particle interactions are a key process at work in Earth's outer radiation belt (e.g. Thorne, 2010; Horne et al., 2016). The high-energy electrons that are trapped in the inner magnetosphere forming the outer belt can have their energy, pitch-angle, and even radial location modified by interactions with a wide range of electromagnetic perturbations (e.g. Green & Kivelson, 2004; Reeves et al., 2013; Lejosne et al., 2022; W. Li & Hudson, 2019; Ripoll et al., 2020).

One of the most well-studied wave-particle interactions in the outer radiation belt is that of whistler-mode waves with electrons (e.g. Horne et al., 2005a; Thorne, 2010; Artemyev et al., 2016; J. Li et al., 2019). This wave mode is typically generated with sufficient frequency range that it can interact with electrons over a broad range of energies (e.g. Horne et al., 2003b; Allison et al., 2021) making the wave-particle interac-

tion particularly effective. In the relatively high-density environment of the plasmasphere, the waves are largely responsible for enhanced scattering of the direction of the electron momentum, which can ultimately lead to loss into the bounce, or drift-bounce, loss cone (e.g. Thorne et al., 1973; Meredith et al., 2006, 2007, 2009; Ni et al., 2013, 2014; Malaspina et al., 2020). In the less dense plasma trough environment, the whistler-mode wave-particle interaction can also lead to energization (heating, also referred to as acceleration) of high-energy electrons (e.g. Horne et al., 2005b). The complex balance between acceleration and scattering in the plasma trough is still under investigation, as it can be significantly affected by the latitudinal distribution of the waves (D. Wang & Shprits, 2019) and in the presence of strong diffusion (Daggitt et al., 2024). Models of radiation belt evolution in time are more successful when energization and scattering by whistler-mode waves is included (e.g. Tu et al., 2013; Glauert et al., 2014a). Finally, observations of developing peaks in phase space density (e.g. Green & Kivelson (2004); Iles et al. (2006); Reeves et al. (2013)) indicates the key importance of whistler-mode waves in the plasma trough. Because of their connection to the detection of whistler-mode waves on the ground with particular characteristics (e.g. Helliwell, 1969; Allcock, 1957), naturally-generated whistler-mode waves in the low-density plasma trough are often referred to as "chorus".

Whistler-mode chorus can be structured in frequency space or relatively broadband and featureless (e.g. W. Li et al., 2012). In the present study, we will refer to all whistler-mode waves detected outside the plasmsphere as "chorus" even though we do not study the frequency structure of the emission. We note that this approach of assuming such waves are chorus is very common in the literature. Chorus emissions have been extensively studied (e.g. W. Li et al., 2011; Cully et al., 2011; Agapitov et al., 2013, 2017; Tao et al., 2021; X.-J. Zhang et al., 2021; Hanzelka & Santolík, 2024) and are likely caused by nonlinear processes within the wave-particle interaction (for a comprehensive review, see Omura, 2021). Structureless emissions outside the plasmapause are often related to the broadband plasmaspheric hiss that occurs inside the plasmasphere (e.g. Zhu et al., 2015, 2019; J. L. Wang et al., 2020; Feng et al., 2023). Whistler-mode chorus are right-hand polarized and can have a range of wave-normal angles (e.g. Agapitov et al., 2013; W. Li et al., 2013; Mourenas et al., 2014; Taubenschuss et al., 2014; W. Li et al., 2016; Agapitov et al., 2018; Hartley et al., 2022). The strength of whistler-mode chorus has long been associated with elevated substorm activity (e.g. Meredith et al., 2001; W. Li et al., 2009; Meredith et al., 2014; Rodger et al., 2016; Meredith et al., 2020; Ma et al., 2023; Wong et al., 2024) and solar wind dynamic pressure (e.g. Jin et al., 2022; Liu & Su, 2023; Tang et al., 2023). Chorus wave power envelopes have length-scales of the order of hundreds of kilometers (Aryan et al., 2016; Agapitov et al., 2017, 2018; S. Zhang et al., 2021) and timescales of around 10 seconds (S. Zhang et al., 2021). In short, a lot is known about magnetospheric chorus wave activity, and the community is well-placed to construct models of the wave-particle interaction to be included in large-scale radiation belt numerical models.

An effective description of wave-particle interactions in numerical models is the quasi-linear diffusion coefficient (e.g. Kennel & Engelmann, 1966; Lemons, 2012; Allanson et al., 2022), bounce-averaged forms of which can be found in e.g. Lyons et al. (1972), Glauert & Horne (2005) and Cunningham (2023). These descriptions of the efficacy of the wave-particle interaction have allowed the effective modeling of radiation belt behavior over a range of different extended time periods: (i) storms that last a few days (e.g. Bourdarie et al., 1997), (ii) extended time periods of months that encompass more than one storm (e.g. Tu et al., 2013; Glauert et al., 2014b), (iii) 1 year (Drozdov et al., 2015) and even (iv) 30 years of observations in the inner magnetosphere (Glauert et al., 2018). Hence a lot of effort to date in outer radiation belt modeling has focused on modeling the diffusion coefficients themselves and how they vary in space and time (e.g. Horne et al., 2013; Ripoll et al., 2014; D. Wang et al., 2019; Ma et al., 2023; Wong et al., 2024).

The spatio-temporal variability of wave-particle interactions on relatively short timescales (e.g. minutes to hours) is an important aspect of models that is not often considered, even though we have evidence that there is a large amount of variability in observations of wave power and other characteristics (e.g. Spasojevic et al., 2015; Murphy et al., 2016; Watt et al., 2017). The consequences of large spatio-temporal variability can be seen in numerical solutions to the Fokker-Planck equation, and has been demonstrated for both radial diffusion (Thompson et al., 2020) and pitch-angle scattering (Watt et al., 2021, 2022). In each case, numerical experiments with different temporal or spatial scales of variability were initiated, resulting in ensembles of Fokker-Planck solutions that demonstrate significant deviations from expected behavior as characterized by an "averaged coefficient" (for an in-depth discussion on appropriate averaging, see Watt et al. (2019) and Ross et al. (2020)). In the case of pitch-angle scattering due to plasmaspheric hiss, numerical experiments showed that rapid variation in the strength of wave-particle interactions with timescales less than 30 minutes resulted in ensembles of solutions that can be effectively described using appropriately-averaged diffusion coefficients. However, for longer timescales of variation, the members of the ensembles deviated significantly from one another, demonstrating a wide range of outcomes (Watt et al., 2021, 2022). A key missing piece of information in the study of the effect of temporal variability of wave-particle interactions is the identification of timescales on which bounce- and drift-averaged diffusion coefficients vary in the inner magnetosphere.

Constructing statistical models of diffusion coefficients remains necessary because wave-particle interactions vary in L^*, magnetic local time and magnetic latitude (e.g. Meredith et al., 2018, etc.). Therefore, even for those events where in-situ measurements exist and event-specific diffusion coefficients can be calculated (e.g. Ripoll et al., 2017, etc.), we are not always guaranteed that the spacecraft providing those event-specific diffusion coefficients have sampled from sufficient magnetic local times or latitudes to construct a global picture of wave activity at that moment. Advances in this area can be made by including statistical information beyond long-term averages (see e.g. Watt et al., 2017; Bentley et al., 2019; Thompson et al., 2020; Watt et al., 2021, for discussion) to describe the variability of the wave-particle interaction in addition to the average levels.

The cause of the spatio-temporal variability of wave and plasma characteristics in the inner magnetosphere is not always fully understood. When the variability of diffusion coefficients has been studied in the past, e.g. for plasmaspheric hiss (Watt et al., 2019), it was clear that parameterization by single parameters such as geomagnetic activity could only slightly reduce the amount of inherent variability in the wave-particle interaction. Since the uncertainty in the Fokker-Planck solutions is related to the amount of variability in the underlying diffusion coefficient model (Thompson et al., 2020), if we cannot reduce the variability through effective parameterization, it is important to faithfully include it in the diffusion coefficient model.

Motivated by recent numerical results, it is our aim to construct statistical models of the spatio-temporal variability of wave activity and plasma conditions such as number density, so that they may be combined to create models of the spatio-temporal variability of diffusion coefficients that can be used in a range of radiation belt models (e.g. Fokker-Planck models like the BAS-RBM (Glauert et al., 2014b) or test-particle models like K2 (Chan et al., 2023)). The spatio-temporal models would reproduce the physical time and length-scales of variability of the underlying wave and plasma environment such that realistic time-series of bounce- and drift-averages of the diffusion coefficients can be created. We are additionally motivated to develop methods to quantify the uncertainty in the solutions to radiation belt models, as is common in weather and climate modeling (see e.g. Tebaldi & Knutti, 2007).

In this paper, we focus in particular on the occurrence rates and spatio-temporal variability of whistler-mode waves in the spatial and temporal region covered by the Van

Allen Probe mission, and those factors that might contribute to their variation. While investigating whistler-mode spatio-temporal variability outside the plasmasphere, we uncovered a methodology for separating different types of whistler-mode waves, and suggest that future models should separate the two different types of chorus waves due to their significant differences.

2 Statistical model-building

Models of quasilinear diffusion coefficients D_{ij} for gyroresonant wave-particle interactions require inputs of plasma and wave properties for their construction (e.g. Glauert & Horne, 2005). Here, i and j could be pitch-angle, or one of either energy or momentum, and i can equal j. The input of the number density and magnetic field strength (and in some cases plasma composition) are required to constrain the resonant condition. The wave properties, including power as a function of frequency and wavevector, further dictate the strength of the wave-particle interaction.

All inputs to the quasilinear diffusion coefficients vary in time and space, but the factors that dictate the different variations are not necessarily the same. For example, dayside magnetospheric reconnection and inner magnetospheric dynamics play large roles in constraining the structure of cold plasma density in the inner magnetosphere (Goldstein, 2006). However, many studies indicate that substorm injections have influence on the activity of whistler-mode waves in the inner magnetosphere (e.g. Meredith et al., 2001; W. Li et al., 2009), hence the factors that control one input to the diffusion coefficient may have a different effect on another. The "ingredients" that are combined to make the D_{ij} can vary on different time and length-scales (e.g. Watt et al., 2021). It is therefore important to consider both individual variation and co-variation of important parameters when building combined models.

Our long-term aim is to construct spatio-temporal models for each input into the quasilinear diffusion coefficients, including any co-dependencies, and then in future work construct a spatio-temporal model of the resulting D_{ij}. In this effort, we define the model domain, or "model-space", as the parameter space in which models of gyro-resonant wave-particle interactions are constructed for use in radiation belt models. Typically, this model-space has coordinates L^*, magnetic local time MLT, and magnetic latitude λ. For our planned spatio-temporal models of diffusion coefficients, we require information about:

- occurrence rates of waves,
- distribution of wave power,
- how wave power varies with wave frequency ω and wave-normal angle θ,
- temporal scales of variation of waves, number density and magnetic field,
- length scales of variation of waves, number density and magnetic field.

In the current work, our initial focus will be on the occurrence rates and wave power of whistler-mode waves found outside the plasmasphere in the region sampled by the NASA Van Allen Probes mission. We will demonstrate how additional statistical analysis of years of observations can allow for better understanding of the spatio-temporal variability of whistler-mode chorus activity in the inner magnetosphere and provide key building blocks for future models.

3 Methods

For this study, we use ~ 7 years of data from the EMFISIS instrument (Kletzing et al., 2013, 2023) on Van Allen Probe A from 7th November 2012 to the end of the mission on 14th October 2019. Although there is plenty of evidence of magnetospheric chorus activity outside of the volume of space sampled by the Van Allen Probes (e.g. Agapi-

tov et al., 2013; Meredith et al., 2012, 2020), we here focus on chorus wave activity in the heart of the outer radiation belt. The extensive and high-quality observations collected by the Van Allen Probes are ideally suited to the task. The database of magnetic field measurements used in this study is described in detail in Wong et al. (2024), and important features of the processing are reiterated here. Magnetic field spectra, measured onboard in the frequency range 2.1 Hz to 11.2 kHz, are mapped to a common frequency scale of ten frequency channels from the lower hybrid frequency f_{LHR} to the electron gyrofrequency f_{ce}. The ten mapped frequency channels have the bounds: (f_{LHR}, $0.1f_{ce}$, $0.2f_{ce}$, $0.3f_{ce}$, $0.4f_{ce}$, $0.5f_{ce}$, $0.6f_{ce}$, $0.7f_{ce}$, $0.8f_{ce}$, $0.9f_{ce}$, f_{ce}). We choose to normalize all wave frequencies to the local electron gyrofrequency and do not map to the equatorial gyrofrequency. Although such mapping is an effective method to study whistler mode waves that are generated at the equator (e.g. Santolík et al., 2010), we choose to normalize instead by local gyrofrequency in case some of the waves detected in the lower frequency bands are not generated in this way. Note that we will analyze waves as a function of magnetic latitude λ (i.e. angular displacement from the magnetic equator) and so this alternative method should not introduce insurmountable problems for interpretation. Instrumental background noise is removed from the magnetic field spectral density using the technique described in Malaspina et al. (2017) and applied in Wong et al. (2022, 2024). In the database, zero power $\mathcal{P} = 0$ is assigned to wave power in each frequency range that is below the background noise as determined above. Each observation is assigned an L^* value using the TS04 reference model (Tsyganenko & Sitnov, 2005) and assuming a local pitch-angle of 90°.

Importantly, to identify the waves as chorus, they must be observed outside the plasmasphere. To flag individual observations as inside or outside the plasmasphere, a number of tests are used. First the wave spectra are checked for the presence of electrostatic electron cyclotron harmonics (ECH). A background subtraction is made to observations from the high-frequency receiver (HFR) instrument on EMFISIS as described in Malaspina et al. (2017). The presence of ECH above this background level indicates that the spacecraft are in the low density environment outside the plasmasphere (Meredith et al., 2004), and intervals are checked to ensure that they have consistent inside/outside identifications for intervals of at least 500 seconds. If the ECH waves fall outside the frequency range of the EMFISIS suite, specifically if the third harmonic band falls below the lower frequency limit of the HFR then a density criterion is used for identification where the spacecraft is assumed to be outside the plasmasphere should the density be lower than $max(10\times(6.6/L)^4, 50.0)$ cm^{-3} (W. Li et al., 2015). Densities are all derived from plasma wave measurements made by the HFR instrument on EMFISIS as described in Kurth et al. (2015). If neither criteria are appropriate to the observation, then it is flagged as "unknown". Further details on the processing of the data are given in Wong et al. (2024). The "unknown" data-points correspond to $< 0.1\%$ of the entire set of Van Allen Probe A observations and will not be used in the following analysis.

We will analyze both occurrence rates and wave power distributions in this work; both can vary with L^*, MLT, magnetic latitude λ and frequency f. We define N as the number of observations in a particular (L^*, MLT, λ) bin, $N_{\rm Ch}$ as the number of observations with $\mathcal{P} > 0$, and $N_{\rm trough}$ as the number of observations positively identified to be outside the plasmasphere in the plasma trough. In the text, we will often use the terminology "occurrence rate" and "probability" interchangeably because it aids comprehension of certain concepts. We here acknowledge that the occurrence rate of observations with particular characteristics during the Van Allen Probe mission is the same as the probability that an observation with those characteristics would occur *so long as* the Van Allen Probes have representatively sampled conditions of the inner magnetosphere during times when the plasmapause retreats well within the Van Allen Probe orbits.

The geomagnetic AE indices are obtained from the OMNI database (Papitashvili & King, 2023).

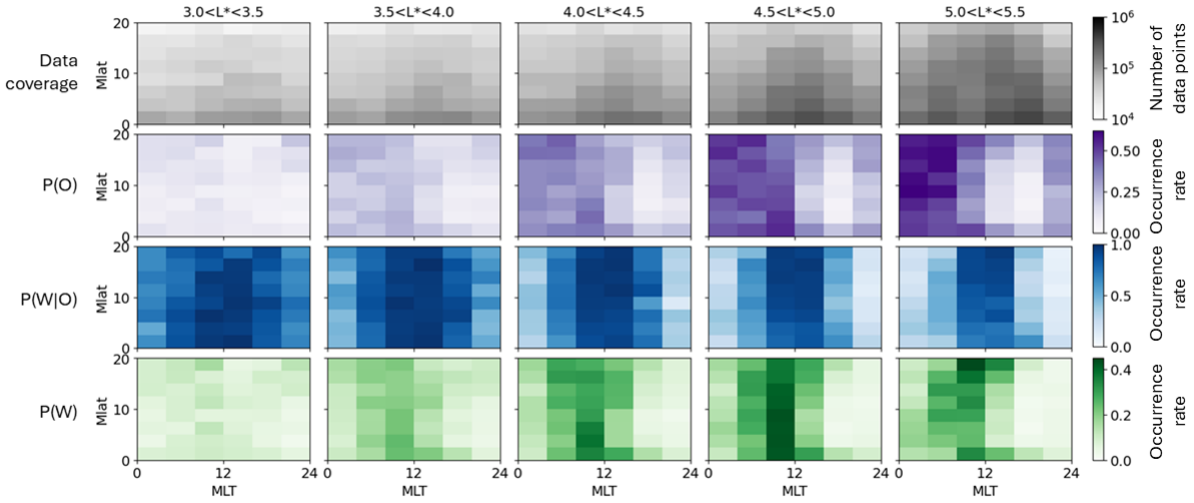

Figure 1. Occurrence rates for conditions in wave observations from Van Allen Probe A for 2012-2019. Each column shows a different L^* range from $L^* = 3.0$ to $L^* = 5.5$ and each panel indicates coverage or occurrence rates as a function of MLT (horizontal axis) and absolute magnetic latitude (vertical axis). [First row] Number of data-points in each $(MLT, Mlat)$ bin (shown using a log-base-10 scale). [Second row] Occurrence rates of positive spacecraft identification outside the plasmasphere N_{trough}/N using the criteria described in the text. [Third row] Occurrence rate of wave power greater than noise for $f_{LHR} < f < 0.5f_{ce}$ when spacecraft is outside of the plasmasphere. [Fourth row] Occurrence rate of wave power greater than noise for $f_{LHR} < f < 0.5f_{ce}$ for entire dataset.

4 Occurrence rates of whistler-mode waves relative to plasmasphere behavior

Our first presentation of whistler-mode occurrence rates as a function of L^*, MLT and λ is shown in Figure 1. We integrate over all lower-band frequencies, from f_{LHR} to $0.5f_{ce}$ in order to obtain a general picture of the occurrence of lower-band whistler-mode waves. Each column of the Figure includes data from a different L^* range in $3.0 \leq L^* \leq 5.5$. Note that although the Van Allen Probe orbits often extend past $L^* = 5.5$, there is insufficient (MLT,λ) coverage to include a column for $5.5 < L^* < 6.0$ that would have data in all bins; we have therefore decided to limit our analysis to $L^* < 5.5$.

The first row of panels in Figure 1 shows the number of data points N in each (MLT,λ) bin on a logarithmic scale. The second row indicates the occurrence rates of times that the spacecraft are identified outside the plasmasphere, which we identify as the probability $P(\mathrm{O}) = N_{\mathrm{trough}}/N$. We note that $P(\mathrm{O}) = 0$ would occur if the spacecraft was never identified outside the plasmasphere, and $P(\mathrm{O}) = 1$ would occur if the spacecraft was always identified outside the plasmasphere in that (MLT,λ) bin for that particular L^* range. The third row shows the occurrence rates of whistler-mode wave power identified above the noise floor should the spacecraft be outside the plasmasphere, which we identify as the probability $P(\mathrm{W|O}) = N_{ch}/N_{\mathrm{trough}}$. In this case, $P(\mathrm{W|O}) = 0$ would correspond to there never being any whistler-mode wave power detected above the noise floor when the spacecraft was identified to be outside the plasmasphere, and $P(\mathrm{W|O}) = 1$ would indicate that every time the spacecraft was outside the plasmasphere, and sampled that (MLT, λ, L^*) bin, whistler-mode wave power above the noise level was detected. Finally, the fourth row shows the occurrence rates of whistler-mode wave signals above

the noise level in each (MLT, λ, L^*) bin, which we identify as the probability $P(\mathrm{W}) = N_{ch}/N$. This probability is equivalent to the occurrence rate of chorus waves in that particular (MLT, λ, L^*) bin, where $P(\mathrm{W}) = 0$ if whistler-mode wave activity is never detected above noise level in that bin, regardless of the number density value, and $P(\mathrm{W}) = 1$ if whistler-mode wave activity is always detected there. The fourth row can also be obtained by combining rows two and three $P(\mathrm{W}) = P(\mathrm{O})P(\mathrm{W}|\mathrm{O})$.

Comparing the second and third row of Figure 1 indicates the importance of separating the two probabilities of 1) being outside the plasmasphere $P(\mathrm{O})$, and 2) observing waves should the spacecraft be outside the plasmasphere $P(\mathrm{W}|\mathrm{O})$. The variation of $P(\mathrm{O})$ (second row) in each L^* shell follows the known shape of the plasmasphere (e.g. Ebihara & Miyoshi, 2011). At low $L^* < 3.5$, it is quite unlikely that the spacecraft will exit the plasmasphere for any MLT, but as L^* increases, the likelihood of exiting the plasmasphere on the dawn side of the Earth grows. Even for $3.5 < L^* < 4.0$, there is a marked difference in the probability of being inside or outside the plasmasphere between dawn and dusk sides of the Earth. For $5.0 \leq L^* < 5.5$, the spacecraft spends nearly 60% of its time outside of the plasmasphere between midnight and 08 MLT where $P(\mathrm{O}) \sim 0.6$, but only 10% of its time outside the plasmasphere between 16-20 MLT where $P(\mathrm{O}) \sim 0.1$. We note here that plasma trough detections on the dusk side of the Earth are low in our analysis coincident with a region where ECH waves are rarely observed (e.g. Meredith et al., 2004; Zhou et al., 2023). Number densities in the inner magnetosphere sampled by the Van Allen Probes also demonstrate similar patterns. Recent work analysing the influence of geomagnetic activity on electron number density indicates that the average electron number density for $L > 5$ and 12-18 MLT is not diminished until activity levels reach $Kp \geq 5$, even though number densities for $L > 5$ and 00-06 MLT are diminished at much lower activity levels $Kp \geq 1$ (Ripoll et al., 2024). Given the statistical distribution of Kp values (e.g. Chakraborty & Morley, 2020; Fiori et al., 2020) both electron number density analysis and the ECH identification used in this paper indicate that plasma trough conditions are observed for $L > 5$ much more often between midnight and noon than they are between noon and midnight.

In the third row, we show the probability of observing whistler-mode waves with power greater than background noise for $f_{LHR} < f < 0.5f_{ce}$ should the spacecraft be identified outside the plasmasphere, i.e. $P(\mathrm{W}|\mathrm{O}) = N_{\mathrm{Ch}}/N_{\mathrm{trough}}$. The probability of detecting wave activity larger than the noise level as a function of MLT and λ (third row) is markedly different than the probability of being inside or outside of the plasmasphere (second row). The occurrence rates of wave activity for all values of L^* are very high, and are centered around noon. Note that the probability color scale on the second row extends $0-0.6$, but the probability color scale in the third row extends up to 1. On the rare occasions that the spacecraft are outside the plasmasphere at low L^*, there is nearly always whistler-mode wave activity on the dayside, and occurrence rates are larger than 0.5 across the remaining MLT and λ sampled by the Van Allen Probe mission. As we move to higher L^*, wave activity is much more restricted to dayside MLT values.

The fourth row of Figure 1 is much more easily understood by considering the multiplication of probabilities in rows two and three. The resulting occurrence rates of lower-band whistler-mode chorus, or, the probability that a high-energy electron would encounter whistler-mode wave activity during its drifting and bouncing path around the Earth, is controlled both by the likelihood of being outside the plasmasphere $P(\mathrm{O})$, and by the likelihood of waves being generated at a particular MLT and λ, $P(\mathrm{W}|\mathrm{O})$. It is also important to remember that as electrons drift around the Earth along their drift-bounce trajectories, the times spent in the pale areas of the fourth row of Figure 1 are likely to be times where they will experience plasmaspheric hiss. The second and fourth rows of Figure 1 indicate that in many circumstances, electrons will experience lower-band chorus for part of their drift-bounce trajectory, and plasmaspheric hiss for other parts. When

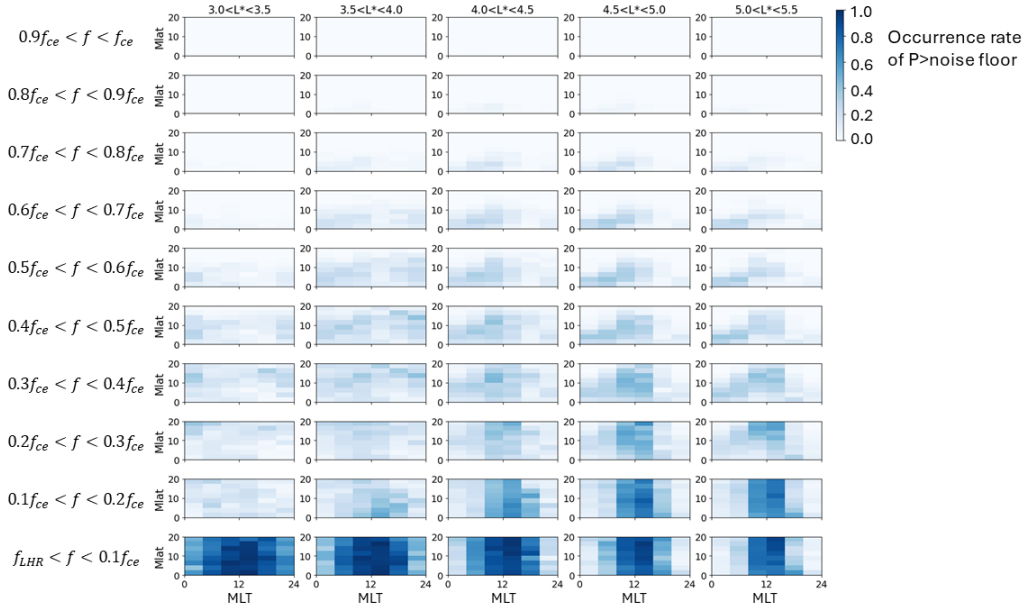

Figure 2. Occurrence rates of wave power greater than noise when spacecraft is outside of the plasmasphere as a function of MLT (horizontal axis of each panel) and λ (vertical axis of each panel). Frequency band increases from bottom row ($f_{LHR} < f < 0.1f_{ce}$) to top row ($0.9 < f/f_{ce} < 1$), and L^* increases from left column ($3.0 < L^* < 3.5$) to right ($5.0 < L^* < 5.5$).

drift-averaging a more detailed spatio-temporal model of diffusion coefficients, as we propose in future, the consequences of these circumstances should be explored.

The inclusion of all whistler-mode wave activity between f_{LHR} and $0.5f_{ce}$ is prompted by work on "low-frequency chorus" (e.g. Meredith et al., 2014), but could be conflating different types of plasmatrough whistler-mode waves, i.e. traditional chorus (e.g. Agapitov et al., 2013; Aryan et al., 2014; Meredith et al., 2020) and exohiss (e.g. Thorne et al., 1973; Zhu et al., 2015; Gao et al., 2018; Zhu et al., 2019; Feng et al., 2023). In what follows, we will separate the wave activity into smaller frequency bands in order to study the occurrence of whistler-mode wave activity in more detail.

5 Statistical wave properties as a function of wave frequency

5.1 Occurrence rates and statistical descriptions of power

Figure 2 shows the occurrence rates of whistler-mode chorus outside the plasmasphere as a function of MLT (horizontal axis of each panel), magnetic latitude (vertical axis of each panel), frequency (row, where lowest frequency band is shown in the lowest row, and highest frequency band is shown in the top row) and L^* (column, with innermost measurements for $3.0 < L^* < 3.5$ in the first column, and high L^* measurements $5.0 < L^* < 5.5$ in the final column). The lowest five rows therefore represent lower-band chorus, and the top five rows show upper-band chorus. The color in the plots represents the occurrence rate of detecting wave power above instrumental noise when the spacecraft is positively identified outside the plasmasphere, i.e. $N_{\mathrm{Ch}}/N_{\mathrm{trough}}$, and varies between 0 and 1.

Studying Figure 2 as a whole, we can see that of the 4 variables L^* (column), f (row), MLT (horizontal axis) and λ (vertical axis), the patterns of chorus occurrence rates vary only slightly with L^*, that is, many columns look very similar, especially the results for $4.0 < L^* < 5.5$.

In general, the occurrence rates of whistler-mode chorus decrease rapidly with increasing frequency, becoming negligible at all (L^*, MLT, λ) for $f/f_{ce} > 0.8$. This is as expected from previous work (e.g. Wong et al. (2024). Occurrence rates are very high in the lowest frequency band, with rates approaching 1 for $08 < MLT < 16$ and for $L^* < 4.5$. Occurrence rates are also high (~ 0.8) for $08 < MLT < 16$, $4.5 < L^* < 5.5$ and $f/f_{ce} < 0.2$.

Concentrating now on the trends in (MLT, λ) for each frequency band, the trends for $L^* < 4.0$ are less clear than those for $L^* > 4.0$, and so we will often focus on the higher L^* range, remembering that N_{trough} is very low for $L^* < 4.0$. The lowest frequency bands show peaks in occurrence rates that are symmetric about noon and vary gently with λ. For higher frequency bands (e.g. $0.4 < f/f_{ce} < 0.6$), the occurrence rate patterns are no longer symmetric about noon. In these frequency ranges, occurrence rates peak close to the equator post-midnight ($00 < MLT < 04$) and peak at higher magnetic latitude near noon. For frequencies $0.2 < f/f_{ce} < 0.4$ there appears to be a mixture of the two occurrence patterns - a symmetric pattern $08 < MLT < 16$ around noon that only varies gradually with λ, and an asymmetric pattern that increases in magnetic latitude with increasing MLT from 00 to ~ 12 MLT.

We next visualize the occurrence rates and wave properties as a function of MLT, λ and f, by combining data at all L^*. This may mask variations at low L^*, since observations outside the plasmasphere are very rare for low L^*. However, Figure 2 indicates that the variations with MLT, λ and f are much more important.

In Figure 3 we have combined observations at all L^*, and investigate wave occurrence rates and wave power as a function of MLT (horizontal axis of each panel), frequency (vertical axis of each panel), and magnetic latitude (row, with $0 < \lambda < 6^\circ$ in the lowest row, $6^\circ < \lambda < 12^\circ$ in the middle row, and $12^\circ < \lambda < 18^\circ$ in the top row). The occurrence rates are shown in the first column, and fall between 0 (no wave activity observed) and 1 (wave activity always observed). The second column shows the median of observations where $\mathcal{P} > 0$. Given the large variability of chorus waves (e.g. Watt et al., 2017), the medians are shown on a log-base-10 scale, where a value of 2.0 is equivalent to $\mathcal{P} = 10^2$ pT^2. The interquartile range (IQR) of the distribution of $\mathcal{P} > 0$ is shown in the third column. We display the IQR of $\log_{10}(\mathcal{P})$ to reflect the large variability in the chorus wave intensity, and it is therefore equivalent to $\log_{10}$ of the interquartile ratio $\mathcal{P}_{75}/\mathcal{P}_{25}$. In the third column, a value of 1 would indicate that there was one order of magnitude between the 25th and 75th percentile. Finally the fourth column shows the total average of observations of wave power in each bin, including $\mathcal{P} = 0$ values. These are calculated in the usual fashion, but displayed using a log-base-10 scale for comparison with the median in the second column. Any white spaces in the second-fourth columns indicate regions of the (MLT, f, λ) model space where the median, average and upper quartile of the wave power are zero.

In panel (i) at low magnetic latitudes (i.e. close to the magnetic equator), there are two separate regions of finite wave occurrence rates covering roughly $06 < MLT < 20$, $f/f_{ce} < 0.3$ (with high occurrence rates $0.8 - 1$) and $00 < MLT < 10$, $0.3 < f/f_{ce} < 0.7$ (with relatively low occurrence 0.2–0.3). In panel (e), for latitudes just off the equator at $6^\circ < \lambda < 12^\circ$, the two wave activity groups are much less separated in MLT. There is still a region of high occurrence rates covering roughly $06 < MLT < 20$, $f/f_{ce} < 0.3$ that neighbors a region of lower occurrence rates covering $02 < MLT < 14$, $0.2 < f/f_{ce} < 0.6$. In panel (a), for the highest latitude bin studied ($12^\circ < \lambda < 18^\circ$), there does not appear to be two separate regions of occurrence rates, just one. This might be

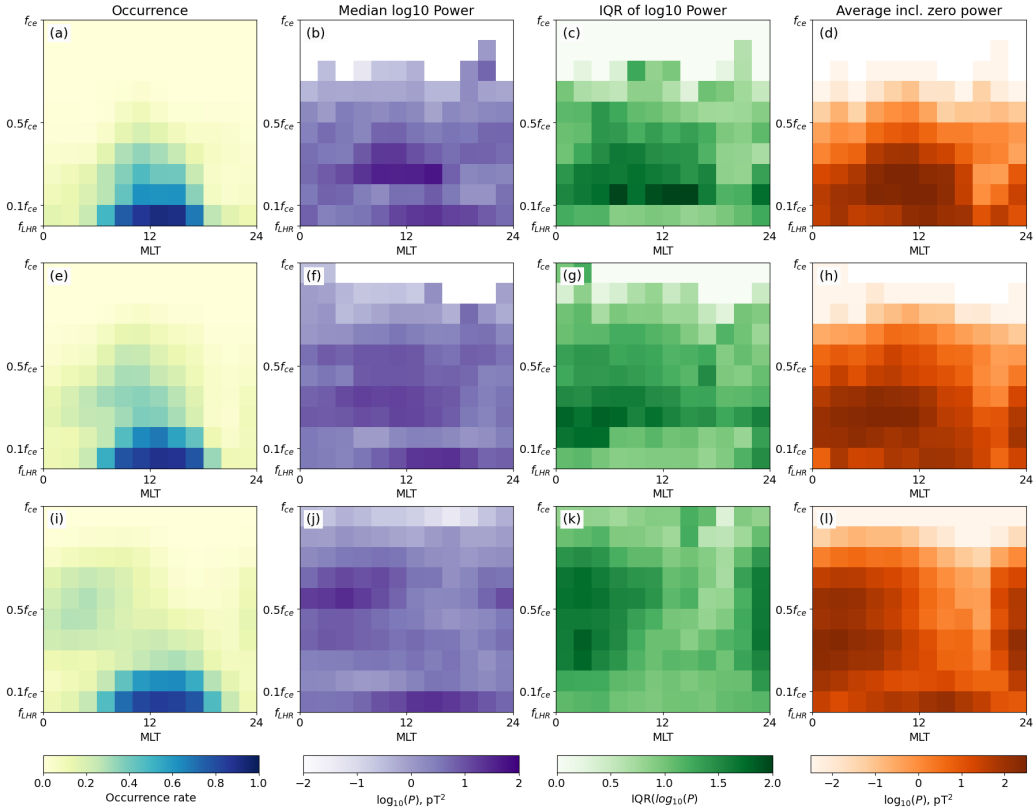

Figure 3. Statistics of chorus wave activity as a function of MLT (horizontal axis of each panel) and frequency (vertical axis of each panel). Frequencies span the range from the lower hybrid resonance f_{LHR} to the electron gyrofrequency f_{ce}. The ratio f_{LHR}/f_{ce} has values in the range 0.016-0.022 for Van Allen Probe observations outside the plasmasphere. Panels (a-d) show statistics from $12^\circ < \lambda < 18^\circ$, (e-h) from $6^\circ < \lambda < 12^\circ$ and (i-l) from $0 < \lambda < 6^\circ$. Occurrence rates of $\mathcal{P}$ are displayed in the first column. Median wave power greater than noise level is displayed in the second column using a log-base-10 scale (so that a value of -2 is equivalent to $\mathcal{P} = 10^{-2}$ pT^2). Interquartile ratio of $log_{10}(\mathcal{P})$ when $\mathcal{P}$ is greater than noise is displayed in the third column. The average wave power, calculated including values of $\mathcal{P} = 0$ when wave power does not exceed instrumental noise, is displayed in the fourth column, also on a log-base-10 scale. In the 2nd, 3rd and 4th columns, values are set to zero if there are fewer than five $\mathcal{P} > 0$ values in that particular (MLT,λ,f) bin.

because there are no longer two different regions of enhanced occurrence rates, or it could be that they significantly overlap in frequency and MLT. The analysis presented later in this paper will investigate these regions of enhanced occurrence rates seen in Figure 3(a,e,i) more closely.

Turning attention to the statistical properties of the waves, near the equator (bottom row: $0 < \lambda < 6°$), the two areas of enhanced wave occurrence rate coincide with the largest median wave power (panel (j)) and the largest average wave power (panel (l)). However, the variability in the wave power (represented by the interquartile range of the log_{10} wave power in panel (k)) is small (< 0.5) for the high-occurrence rate region at $06 < MLT < 20$, $f/f_{ce} < 0.3$, but much larger (1.5-1.75) for the lower-occurrence rate region at $00 < MLT < 10$, $0.3 < f/f_{ce} < 0.7$.

At higher latitudes, the pattern repeats. High values of median and average wave power (columns 2 and 4) coincide with regions of enhanced wave occurrence rates (column 1), although as mentioned before, the regions of high wave power and occurrence rates merge in (MLT, f)-space as latitude increases. At all latitudes, there remains a region of low wave variability for $06 < MLT < 20$ and low frequency. As latitude increases, the region of low variability around noon occupies a diminishing range of frequency.

We provide additional Figures in the Supplementary Information that show the occurrence rates, median and IQR of the waves as a function of L^*. These Figures indicate that the statistics for $4.0 < L^* < 5.0$ and $5.0 < L^* < 6.0$ are quite similar to those shown in Figure 3 but those for $3.0 < L^* < 4.0$ are quite different. The very small number of events recorded outside the plasmasphere for $3.0 < L^* < 4.0$ will not contribute greatly towards the conclusions of this study, but should not be ignored when constructing statistical models of wave behavior across the inner magnetosphere.

5.2 Comparison between wave statistics and previous works

Many studies have determined different aspects of the statistical distribution of whistler-mode wave power in the Earth's magnetosphere, including W. Li et al. (2009, 2010); Agapitov et al. (2011); Meredith et al. (2012); Agapitov et al. (2013); Tyler et al. (2019); Meredith et al. (2020). Some reported occurrence statistics (e.g. Agapitov et al., 2011; Tyler et al., 2019), and many reported maps of average wave activity (e.g. W. Li et al., 2009, 2010; Meredith et al., 2012, 2020). The statistical occurrence rates determined in Agapitov et al. (2011) are similar to those we show in Figures 2 and 3, although we show more detail in magnetic latitude and frequency band. Both Agapitov et al. (2011) and the results in Figure 3 demonstrate that occurrence rates tend to peak on the dayside and large occurrence rates can persist into the post-noon sector. Averaged maps tend to give the impression that lower-band whistler-mode wave activity near the equator extends from 00-12 MLT, and peaks between 06-12 MLT (e.g. W. Li et al., 2009; Meredith et al., 2012). We note from Figure 3 that the pattern of occurrence rates (first column) can be quite different from an averaged map (final column), and in this section we explore this in more detail.

We isolate waves in a single frequency band $0.1 < f/f_{ce} < 0.2$ and select those close to the magnetic equator ($|\lambda| < 6°$). In Figure 4 we show histograms of all 6s whistler-mode power observations in this frequency band for $\mathcal{P} > 0$. Occurrence rates for $\mathcal{P} > 0$ in each (MLT,λ) bin are shown in the title of each panel (a-d). It is important to note that the horizontal axis is $\log_{10} P$ and so a value of 2 corresponds to 10^2 pT^2, and a value of 4 is two orders of magnitude larger at 10^4 pT^2. The histogram at 02-04 MLT has a pronounced heavy tail, with some values exceeding 10^5 pT^2. In contrast, the histograms at 10-12 MLT and 14-16 MLT indicate that power values here rarely exceed 10^3 pT^2. The median and 75th percentile of the $\mathcal{P} > 0$ values are shown using blue dashed lines

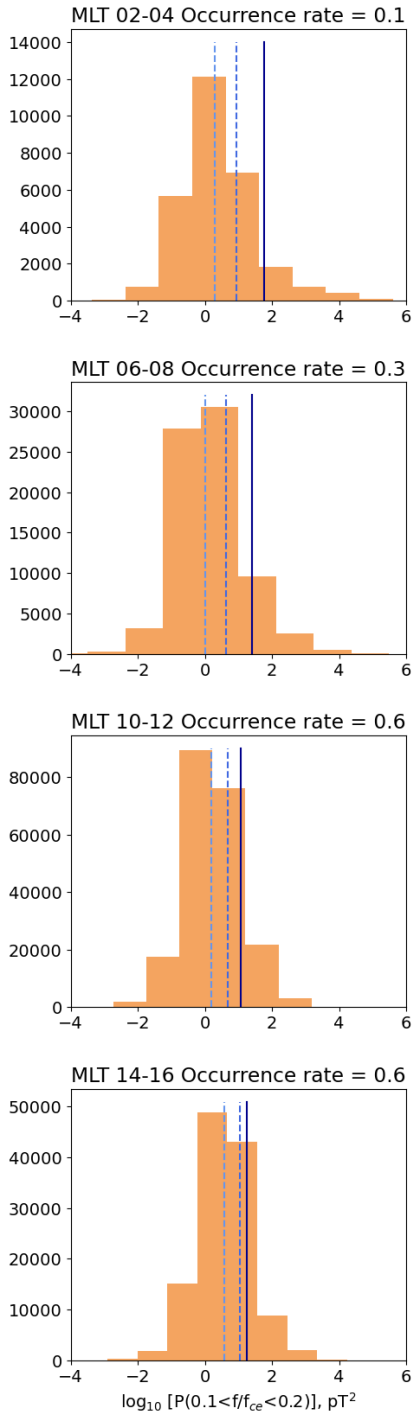

Figure 4. Histograms of chorus wave power when $\mathcal{P} > 0$ for frequency band $0.1 < f/f_{ce} < 0.2$ and magnetic latitude $|\lambda| < 6^\circ$ for (a) 02-04 MLT, (b) 06-08 MLT, (c) 10-12 MLT and (d) 14-16 MLT. Dashed blue lines indicate the median and 75th percentile of the $\mathcal{P} > 0$ values. The solid line indicates the average value *including* the $\mathcal{P} = 0$ values.

in each panel; these do not vary much with MLT. The occurrence rates increase with MLT, from a low value of 0.1 at 02-04 MLT to a value of 0.6 for 10-12 MLT and 14-16 MLT.

The average wave power in this frequency band, including the $\mathcal{P} = 0$ values, is indicated in each panel with a solid blue line. The average wave power, as used to construct statistical maps like those in W. Li et al. (2009, 2010); Meredith et al. (2012, 2020) is a combination of the wave power and the occurrence rate since it includes the $\mathcal{P} = 0$ values. We can see that the average wave power *reduces* with MLT, even as the wave occurrence rates increase. Waves are detected above the noise level much more often at larger MLT, but never display the high power observed at lower MLT in the post-midnight sector.

The significant changes in the distribution of wave power and wave occurrence rates between 02-04 MLT and 10-12 MLT results in the averaged wave power maps often presented in the literature. However, the averaged wave power in the post-midnight sector remains much smaller than the very large values of power that have been the subject of other studies (e.g. Cattell et al., 2008; Wilson III et al., 2011; Tyler et al., 2019) and can be seen in the long statistical tail of power in Figure 4(a).

Guided by previous numerical studies of the consequences of temporal variations in diffusion coefficients (Thompson et al., 2020; Watt et al., 2021, 2022), we suggest that the consequences of wave-particle interactions with high-power waves that exist a small fraction of the time (see Figure 4 and Tyler et al., 2019) may be very different to the consequences of wave-particle interactions with much less strong waves that exist $> 50\%$ of the time. Thompson et al. (2020) demonstrated that the numerical solutions to the Fokker-Planck equation depended upon the amount of variability in the underlying distribution of diffusion coefficients, in addition to the shape of the distribution of diffusion coefficients. The statistics presented here will contribute towards future numerical experiments to determine the importance of the occurrence rates and distributions of whistler-mode wave activity in the plasmatrough.

6 Wave Spatio-temporal Variability

Evidence from near the equator indicates that there may be two different unconnected regions of wave activity, but that these regions overlap in frequency at higher latitude. This section uses the differences in wave variability, motivated by column 3 of Figure 3, to determine whether there are any differences in the two wave activity regions.

6.1 Variability in the spatio-temporal series of spacecraft observations

We first visualize the spatio-temporal variability of chorus wave activity in the two regions of (MLT, λ, f) that seem separated at low magnetic latitude $|\lambda| < 6^\circ$ in Figure 3(i); the post-midnight sporadic region at relatively high frequency relative to f_{ce}, and a dayside near-continuous region at relatively low frequency. Figure 5(a) shows an example interval of the wave power spectral density from the EMFISIS instrument on Van Allen Probe A, when the spacecraft was in the post-midnight equatorial region $\lambda \sim 3^\circ$ and $MLT \sim 05$. Dotted and dashed lines indicate the frequency boundaries used in this study from f_{LHR} up to $0.6 f_{ce}$ where we reiterate that these are local values, not mapped equatorial values. The dashed lines indicate $0.5 f_{ce}$ and $0.6 f_{ce}$ which delimit the power displayed in panel (c) during the same interval. In comparison, Figure 5(b) shows an example interval of whistler-mode wave power spectral density from the dayside at $MLT \sim 11$. Again, dashed and dotted lines show the frequency boundaries used in this study, and the dashed lines now show the frequency limits for panel (d): f_{LHR} and $0.1 f_{ce}$. The most striking difference between the two examples of spatio-temporal observation series is the amount of variability from one 6s sample to the next. For the waves observed in the post-midnight region (Figure 5(c)), there are large amounts of variability in the

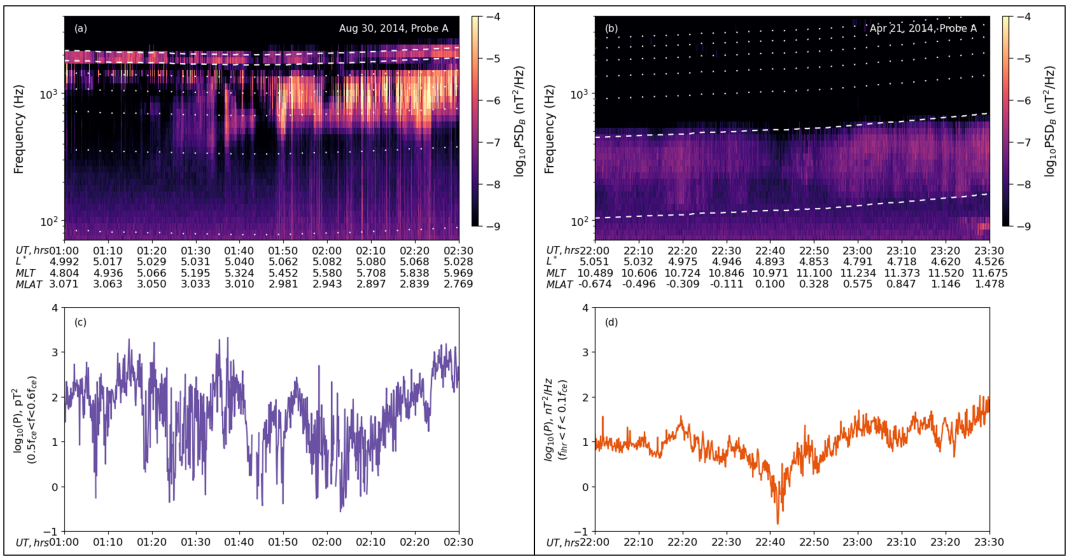

Figure 5. (a,c) Example interval of spatio-temporal variability of post-midnight equatorial whistler-mode wave activity: (a) Wave power spectral density from Van Allen Probe A on August 30, 2014. Dashed white lines indicate the frequencies $0.5f_{ce}$ and $0.6f_{ce}$ which delimit the wave power shown in panel (c). Dotted white lines indicate the other important frequencies that delimit wave power in this study: f_{LHR}, $0.1f_{ce}$, $0.2f_{ce}$, $0.3f_{ce}$ and $0.4f_{ce}$. The colorscale has a ceiling at 10^{-4} nT^2/Hz to highlight variability in $0.5 < f/f_{ce} < 0.6$ band. (b) $\log_{10}(\mathcal{P}(0.5 < f/f_{ce} < 0.6))$ during the interval identified in panel (a), where $L^* \sim 5$, $MLT \sim 05$ and $\lambda \sim 3°$. (b,d) Example interval of spatio-temporal variability of dayside equatorial whistler-mode wave activity: (b) Wave power spectral density from Van Allen Probe A on April 21, 2014. Dashed white lines indicate frequencies f_{LHR} and $0.1f_{ce}$, which delimit the wave power shown in panel (b). Dotted white lines indicate frequencies: $0.2f_{ce}$, $0.3f_{ce}$, $0.4f_{ce}$, $0.5f_{ce}$ and $0.6f_{ce}$. Colorscale has a ceiling at 10^{-4} nT^2/Hz to compare with August 30, 2014 interval. (d) $\log_{10}(\mathcal{P}(f_{LHR} < f < 0.1f_{ce}))$ during the interval identified in panel (b), where $L^* \sim 4.7$, $MLT \sim 11$ and $\lambda \sim 0°$.

signal, and the power in one sample is not strongly related to the power six seconds later. For the waves observed in the dayside region (Figure 5(d)), there is much smaller variability in the spatio-temporal series, and each 6s sample is much more similar to the next sample. In other words, some of the variability differences seen in Figure 3(k) between post-midnight and daytime waves are occurring on timescales as short as ~ 6 s. We remind the reader that the 6s sampling of wave power spectral density by the EMFISIS instrument involves a calculation of power spectral density over a 0.5s interval every 6s (Kletzing et al., 2023).

We approximate the variability in short sub-intervals of data using the inter-quartile range (IQR) of $\log_{10}(\mathcal{P})$ over time intervals that allow us to combine multiple 6s samples. We have analyzed intervals of 2 minutes (20 data points), 5 minutes (50 data points) and 10 minutes (100 data points), and there is little substantive difference in results. We proceed with 5 minute intervals as it provided the best separation in the results that follow. We also note that other measures of variability exist (e.g. the coefficient of variation), but interpretation of such measures often rests upon assumptions of Gaussian or log-Gaussian distributions. The IQR of $log_{10}(\mathcal{P})$ has the benefit of being easy to interpret, and makes no assumptions regarding the underlying distribution of values. Using the IQR of $log_{10}(\mathcal{P})$ results in inherent normalization of the variability, since it describes the number of orders of magnitude between the 25th and 75th percentile. Hence variability that spans values of, say, 10^0 pT^2 and 10^1 pT^2 would result in the same value of $IQR(\log_{10}(\mathcal{P}))$ as variability that spans values of 10^2 pT^2 and 10^3 pT^2.

We calculate the IQR of $\log_{10}(\mathcal{P})$ in each frequency band for contiguous 5-minute intervals of wave power throughout the entire dataset, discarding a wave interval at a particular frequency if more than 20% of samples are missing because the spacecraft is passing from inside to outside the plasmasphere, or if more than 25% of wave power in that 5-minute interval is indistinguishable from noise, since that results in a lower quartile of zero and makes the log_{10} operation problematic. The distribution of IQR for $0.5 < f/f_{ce} < 0.6$ in the post-midnight low-latitude region (i.e. $|\lambda| < 6^\circ$ and $00 < MLT < 08$) is shown in Figure 6(a), and the distribution of IQR for $f_{LHR} < f < 0.1 f_{ce}$ in the dayside low-latitude region (i.e. $|\lambda| < 6^\circ$ and $08 < MLT < 20$) is shown in Figure 6(b). The IQR of the higher frequency post-midnight intervals is typically significantly greater than 0.5, whereas the IQR for the lower frequency dayside waves is typically significantly less than 0.5. We note that the spread of IQR values is very large for the post-midnight intervals is also much larger than the spread of IQR values for the dayside intervals. The two regions of enhanced occurrence rates near the equator (see Figure 3(i)) exhibit very different variabilities over 5-minute intervals.

6.2 The dependence of low-variability dayside equatorial waves and high-variability post-midnight equatorial whistler-mode waves on substorm activity

In the previous section we showed that near equatorial magnetic latitudes, low-frequency whistler-mode waves with high occurrence rates that occur on the dayside of the magnetosphere tended to exhibit low variability in wave power during five minute windows (hereafter termed "low-variability waves"). Higher-frequency whistler-mode waves that are more sporadic and found in the post-midnight sector exhibit high variability during five-minute intervals (hereafter termed "high-variability waves"). In this section, we determine whether there are further differences between the two wave types. In this subsection, we will continue our focus on equatorial latitudes ($0 < \lambda < 6^\circ$), before moving on to analyze all waves in section 6.3.

Many previous studies have indicated evidence for a dependence of whistler-mode waves activity on substorm activity (e.g. Meredith et al., 2001; W. Li et al., 2009, 2011; Meredith et al., 2014, 2020; Ma et al., 2023; Wong et al., 2024). In Figure 7, we inves-

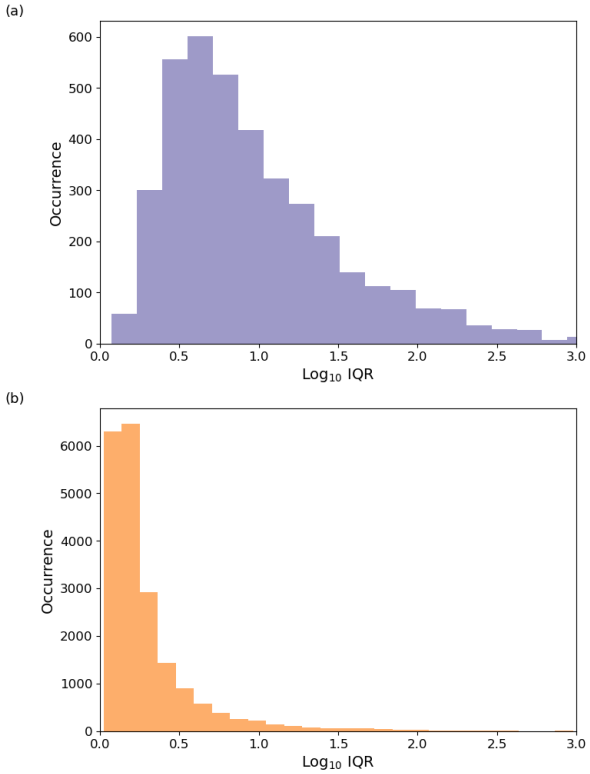

Figure 6. Histograms of the IQR of $log_{10}(\mathcal{P})$ for 5-minute intervals during the entire Van Allen Probe A dataset subject to the following constraints: Each 5-minute interval must have $> 80\%$ 6s samples positively identified to be outside the plasmasphere, $> 75\%$ of 6s samples must have $\mathcal{P} > 0$. The 5-minute intervals were additionally chosen to satisfy (a) $0.5 < f/f_{ce} < 0.6$, $|\lambda| < 6^{\circ}$, $00 < MLT < 08$ and (b) $f_{LHR} < f < 0.1 f_{ce}$, $|\lambda| < 6^{\circ}$, $08 < MLT < 20$

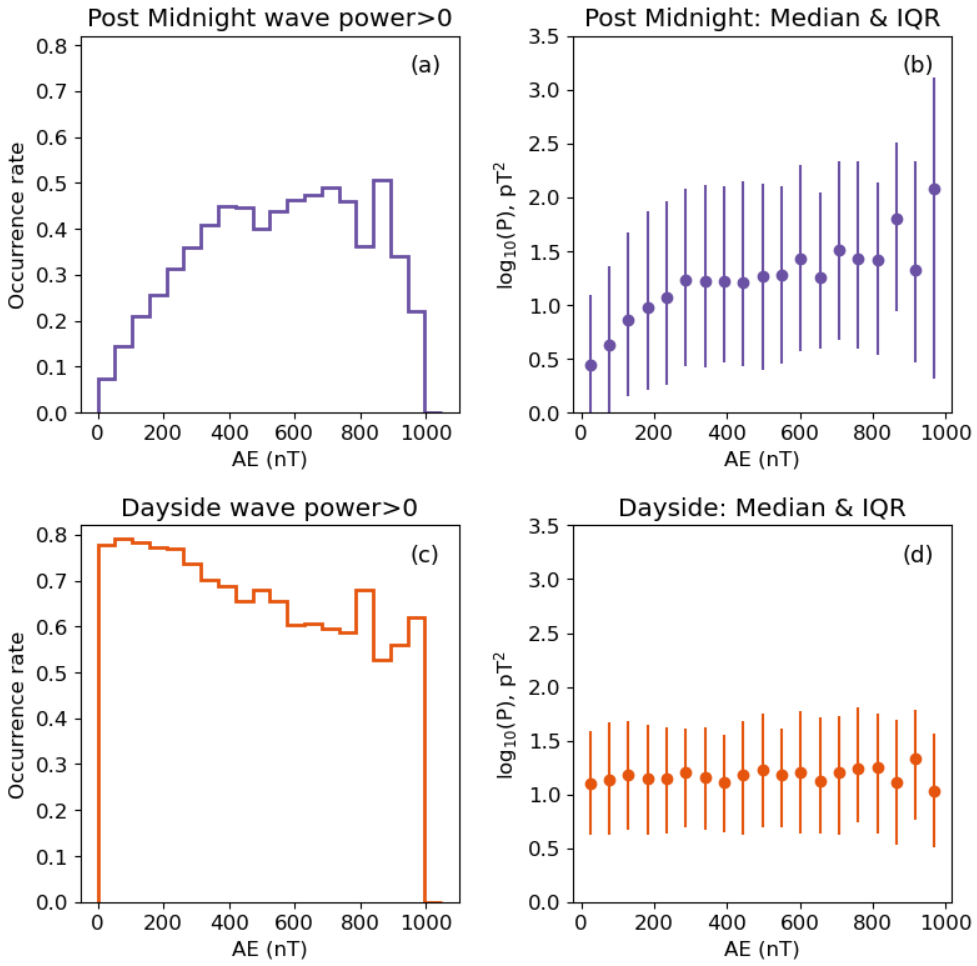

Figure 7. Dependence of whistler-mode wave activity on the AE index for two different regions of the magnetosphere and two different frequency bands: First row shows dependence on the AE index of (a) the occurrence rates of $\mathcal{P}(0.5f_{ce} < f < 0.6f_{ce})$ greater than noise and (b) the values of $\mathcal{P}(0.5f_{ce} < f < 0.6f_{ce})$ greater than noise for $|\lambda| < 6^\circ$ and $00 < \text{MLT} < 08$. Second row indicates dependence on the AE index of (c) the occurrence rates of $\mathcal{P}(f_{LHR} < f < 0.1f_{ce})$ greater than noise and (d) the values of $\mathcal{P}(f_{LHR} < f < 0.1f_{ce})$ greater than noise for $|\lambda| < 6^\circ$ and $08 < \text{MLT} < 20$. In (b) and (d), medians are indicated by circles and IQR are indicated by vertical lines. Units of log-base-10 power are pT^2.

tigate the dependence of both high-variability and low-variability types of waves on the geomagnetic activity index AE (extracted from NASA/GSFC's OMNI data set through OMNIWeb (Papitashvili & King, 2023)). AE is chosen to make meaningful comparison with previous work (e.g. W. Li et al., 2009; Meredith et al., 2012, 2020) and we note that we also investigate AE^* and time-lagged AE in Figure S1. The analysis in Figure 7 compares high-variability waves with frequencies $0.5 < f/f_{ce} < 0.6$ in the post-midnight sector ($00 < \text{MLT} < 08$) in panels (a) and (b) with low-variability waves with frequencies $f_{LHR} < f < 0.1f_{ce}$ on the dayside ($08 < \text{MLT} < 20$) in panels (c) and (d). The occurrence rates of the waves (Figure 7(a) and (c)) is shown, in addition to the wave power (Figure 7(b) and (d)), where filled circles indicate median power, and the vertical lines indicate the extent of the IQR. In all panels, the occurrence rates or power of five minute intervals of whistler-mode wave activity is indicated as a function of instantaneous AE.

Considering first the occurrence rate of five-minute intervals of waves, we see that the occurrence rates of the high-variability waves in the post-midnight sector increases with AE (Figure 7(a)), but the occurrence rate of low-variability waves on the dayside decreases with AE (Figure 7(c)). The occurrence rate of high-variability waves increases dramatically from < 0.1 to around 0.5 for $0 < AE < 400$ nT, but beyond that, there is little further increase in occurrence rates as AE increases to 750 nT. (Note that although the plots span $0 < AE < 1000$ nT, the number of points in the highest activity bins is relatively small and so we will try to avoid over-interpretation of the results in these bins.) In contrast, the occurrence rate of low-variability waves is ~ 0.8 for $AE = 0$, and decreases to ~ 0.6 at $AE = 750$ nT.

The power of high-variability waves varies with AE (Figure 7(b)); median wave power rises from $\sim 10^{0.7}$ pT^2 to $\sim 10^{1.7}$ pT^2 as AE climbs from ~ 0 to ~ 300. However, there is no further climb after this, and the IQR of the power is very large at all values of AE. We note that for other related wave modes such as plasmaspheric hiss, the variability remained large even after parameterizing by geomagnetic index (c.f. Watt et al., 2019). The behavior of high-variability waves shown here supports previous parameterization choices for whistler-mode chorus , where AE is often split into windows $AE < 100$ nT, $100 < AE < 300$ nT, and $AE > 300$ nT (see e.g. W. Li et al., 2009, 2010; Meredith et al., 2020), but we reiterate that there is a large amount of variability not captured by this parameterization (c.f. Watt et al. (2019)). There appears to be no relationship between instantaneous AE and the low-variability wave power (Figure 7d). We note that instantaneous AE may not be the most effective parameter for studying waves at different MLT values, and will extend our analysis to different treatments of AE in the next section, where we will look at all low and high-variability whistler-mode waves outside the plasmasphere in our dataset.

6.3 Using the spatio-temporal variability to identify different "types" of waves

We noted above, relative to Figure 5, that there were systematic differences in IQR between post-midnight equatorial sporadic whistler-mode waves with frequencies $0.3 < f/f_{ce} < 0.7$, and dayside low-frequency whistler-mode waves with frequencies $f_{LHR} < f < 0.2f_{ce}$ whose occurrence rates are much higher. Prompted by these differences, we choose a threshold IQR value of 0.5, and analyze all five-minute chorus wave intervals to determine similarities and differences in behavior across the Van Allen Probes sampling region.

First, we analyze differences between the two types of waves across all five-minute intervals in L^*, MLT and λ that are identified to be outside the plasmasphere. In Figure 8 (a) we show that low-variability waves (orange histogram) have a statistically different frequency profile to the high-variability waves (purple histogram). As expected from our initial analyses, low-variability waves tend to have much lower frequencies than

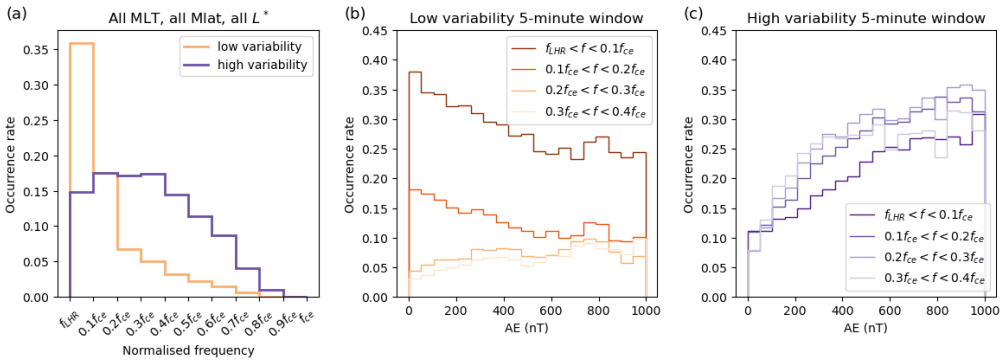

Figure 8. (a) Histogram of whistler-mode wave occurrence for all MLT, λ and L^* as a function of frequency band for low variability waves (orange) and high variability waves (purple). (b) Variation in occurrence rates of low-variability waves as a function of AE for all MLT, λ and L^* in 4 different frequency bands. (c) Variation in occurrence rates of high-variability waves as a function of AE for all MLT, λ and L^* in 4 different frequency bands.

high-variability waves. It is important to remember that we have normalized our wave frequencies to the local gyrofrequency, and leave further analysis of frequency with magnetic latitude to Figure 9.

Figure 8(b) and (c) indicate how the occurrence rate of low-variability and high-variability waves changes with AE. We deliberately chose four frequency channels in which the low-variability and high-variability wave activity overlap, and these lie between f_{LHR} and $0.4f_{ce}$. For the low-variability waves (Figure 8(b)), the two lowest frequency bands decrease in occurrence rate as a function of AE. Note that the occurrence rates are much lower than in Figure 3 because these have been calculated over all L^*, MLT and λ. However, for all high-variability wave bands shown in Figure 8(c), occurrence rates increase with AE. Regardless of where they occur, low variability waves occur less often as AE increases, and high variability waves occur more often as AE increases. The different dependence of occurrence rates indicates that we have identified a way to distinguish waves with very different system-level behavior.

We have also investigated how low and high-variability waves depend on other treatments of AE which account for the time taken for electrons to drift around the inner magnetosphere following substorm injection (see Figure S1 in the Supporting Information). We used instantaneous AE, AE lagged by 3 hours, and AE^* (i.e. the maximum value of AE in the previous 3 hours) and performed the same analysis as in Figure 8. All analyses demonstrate the same behavior: the occurrence rate of low-frequency low-variability waves decreases with AE, whereas the occurrence rate of high-variability waves increases with AE.

Figure 9 shows the occurrence rates of chorus waves as a function of MLT (horizontal axis), frequency (vertical axis) and magnetic latitude (row). In the first column, we show occurrence rates for all five-minute intervals identified outside the plasmasphere (the same as shown in Figure 3). The second column shows low-variability waves, and the third column shows high-variability waves. When the wave intervals are split by IQR, we see that low-variability waves occupy the same region in MLT, and occur at the same normalized frequencies across all magnetic latitudes in panels (b), (e) and (h).

In contrast, the high-variability waves vary strongly with MLT, normalized frequency and λ, in a similar way to that suggested by the high-IQR regions of the third column

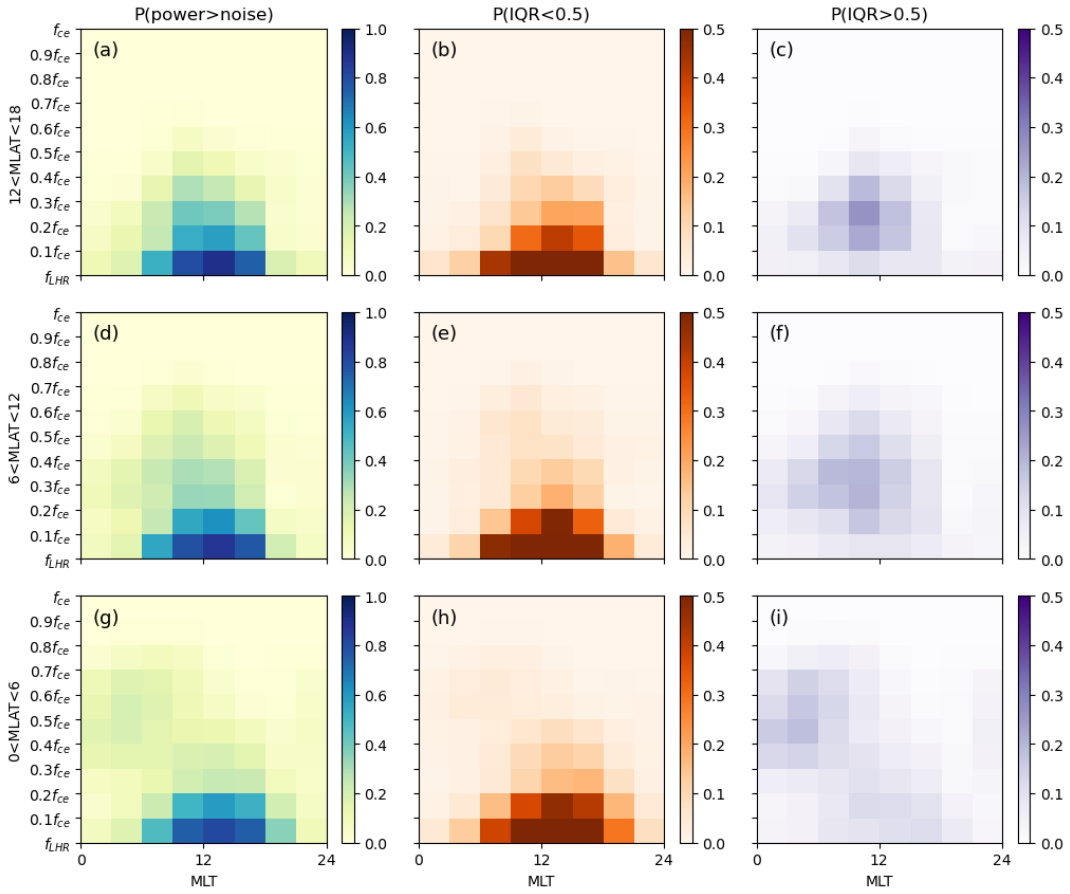

Figure 9. Occurrence rates of whistler-mode waves as a function of MLT (horizontal axis), normalized frequency (vertical axis) and magnetic latitude (row, with $0 < \lambda < 6^\circ$ in the bottom row, $6^\circ < \lambda < 12^\circ$ in the middle row and $12^\circ < \lambda < 18^\circ$ in the top row). The first column (panels a, d, and g) show occurrence rates of whistler-mode wave activity for all five-minute intervals where the spacecraft is determined to be outside the plasmasphere, the second column (panels b, e, and h) shows occurrence rates for low-variability waves, and the third column (panels c, f and i) shows occurrence rates for high-variability waves. Note that the color-scales of the second and third columns have been fixed between 0.0 and 0.5 in order to compare the different wave types. Wave occurrence rates in the second column for the lowest frequency bands are therefore saturated.

of Figure 3. In the immediate post-midnight region (00−03 MLT), high-variability waves occur more frequently at low-latitudes (Figure 9i), with very little wave activity at mid-latitudes (Figure 9c and f). As MLT increases (03−09 MLT), we see occurrence rates of ~ 0.2 at all latitudes, but with normalized frequencies that decrease with latitude. Around noon (09−18 MLT), the behavior of high-variability waves changes. There are low occurrence rates near the equator at low frequency ($f < 0.2 f_{ce}$), and higher occurrence rates at higher latitude at higher normalized frequencies ($0.2 < f/f_{ce} < 0.6$).

The two wave activity regions in Figure 9(g) are not completely separated at all latitudes using this method, as can be seen clearly for the high variability waves in panel (i). However, the low-variability waves appear to be effectively isolated in panels (h), (e) and (b), and the high-variability waves appear to be effectively isolated in panels (f) and (c) (where $6^\circ < \lambda < 18^\circ$).

The low-variability waves in the second column do not show much variation in normalized frequency with magnetic latitude, i.e. the frequency coverage of Figure 9(b), (e) and (h) is similar. In contrast, the high-variability waves in the third column tend to have lower normalized frequencies at higher latitudes. We suggest that the high-variability whistler-mode waves have the expected normalized frequency dependence on latitude that suggests the source region is localized near the equator and waves then propagate to higher latitudes. Further analysis may be required for the low-variability waves since wave occurrence patterns in frequency are the same regardless of latitude (for the limited magnetic latitude range covered by the Van Allen Probe spacecraft).

We note that we have used frequency normalized to the *local* gyrofrequency in our analysis. Other studies (e.g. W. Li et al., 2009; Santolík et al., 2010; Agapitov et al., 2011) normalize chorus wave frequencies to the estimated simultaneous equatorial gyrofreqency on that field line, obtained through magnetic field modeling. If we had made the choice to normalize by equatorial gyrofrequency in this study, then it is likely that the low-variability waves in the second column of Figure 9 would appear to change their normalized frequency with magnetic latitude, exhibiting higher normalized frequencies at higher magnetic latitude. In contrast, the high-variability waves in the third column of Figure 9 would likely span a similar frequency range at all magnetic latitudes. Both methods of normalization introduce apparent changes in the frequency range of one of the wave types as a function of magnetic latitude. We stress here the importance of retaining the magnetic latitude coordinate in the analysis, regardless of normalization factor chosen.

7 Exohiss and Substorm-driven chorus

The behavior of the high-variability whistler-mode waves detected outside the plasmasphere suggests that these are likely to be traditional substorm-driven chorus (e.g. Meredith et al., 2001; W. Li et al., 2010). These waves are observed sporadically, and both occurrence rates and wave power increase with AE up to $AE \sim 350$ nT, before reaching some kind of plateau in occurrence and wave power (see Figure 8(c)). At low-latitude ($0 < \lambda < 6^\circ$) waves occur in the post-midnight region $00 < \text{MLT} < 08$ with frequencies $0.3 < f/f_{ce} < 0.7$ (see Figure 8(i)). As MLT increases, high-variability waves are seen at successively higher magnetic latitude, and at lower frequency relative to the local gyrofrequency (see Figure 8(c) and (f)) (c.f. Meredith et al. (2020)). Extensive observations and modeling indicates that whistler-mode chorus originates near, or grows most strongly at, the magnetic equator (Muto & Hayakawa, 1987; Muto et al., 1987; Nagano et al., 1996; LeDocq et al., 1998; Hospodarsky et al., 2001; Watt et al., 2012, 2013). Indeed, some statistical studies of whistler-mode chorus use mapped equatorial gyrofrequency to normalize the frequency of emissions to take this behavior into account (e.g. Santolík et al., 2014). Our classification of high-variability waves reveals behavior that has been observed in previous studies (e.g. Meredith et al., 2020), where growth due to

temperature anisotropy (e.g. W. Li et al., 2010; Watt et al., 2012, 2013) is balanced by Landau damping due to suprathermal electrons (e.g. Bortnik et al., 2007) both of which have been characterised as a function of MLT.

The location and behavior of low-variability waves is very different. When considered in the context of previous work, the evidence presented in the current study suggests that low-variability waves detected outside the plasmasphere are most likely to be exohiss (Zhu et al., 2015, 2019; J. L. Wang et al., 2020; Feng et al., 2023; Seo & Kim, 2023) since they occur predominantly at low frequencies and on the dayside (see e.g. Figure 9(b), (e) and (h)). By basing our classification of the waves on their variability during a five-minute window, we avoid the need to classify the wave activity based upon absolute frequency values, and we can see that low-variability waves can have frequencies up to around $0.3f_{ce}$. It is interesting that in our analysis, the occurrence rates of the low variability waves reduces with AE (Figure 8(b)), and the power appears independent of AE. Spasojevic & Inan (2010) study ground-based detections of chorus waves and report that those waves detected at MLT < 10 displayed a stronger dependence on geomagnetic activity than those waves detected at MLT > 10. For Zhu et al. (2019), the occurrence rates peaked at $Kp = 2$. These differences may be explained through the different indices used to quantify geomagnetic activity, but previous work and this study clearly demonstrate that there are different types of whistler-mode waves present outside the plasmasphere, and they are driven by different factors. Our variability-based method of classification will allow a full study of the possible factors that may control the behavior of low-variability waves and will be pursued in future.

We compare the results of this study with those that also include statistical studies of wavenormal angle (e.g. W. Li et al., 2016; Seo & Kim, 2023; Wong et al., 2024). Exohiss, where defined as wave emissions below $0.1f_{ce}$ (Seo & Kim, 2023), largely occurs on the dayside with wavenormal angles less than 20°. For whistler-mode waves detected outside the plasmasphere between pre-midnight and dawn, previous work indicates that these are a mixture of low wavenormal angles and oblique waves (e.g. Wong et al., 2024; W. Li et al., 2016).

It is interesting to note that some author teams (e.g. Seo & Kim, 2023; Feng et al., 2023) have documented difficulties with positively identifying exohiss, especially distinguishing it from other types of whistler-mode emission. Typically, a frequency condition is used, e.g. selecting only wave activity $f < 0.1f_{ce}$ as exohiss. Our analysis (Figure 9) indicates that using a frequency condition would group wave activity that has the occurrence and variability characteristics similar to exohiss alongside traditional chorus (see e.g. Figure 9e). In fact, scrutiny of the interval shown in Figure 5(a) indicates that waves in the lowest frequency band ($f_{LHR} < f < 0.1f_{ce}$ between the two lowest dotted lines) have very low variability in power from the beginning of the interval up to around 01:45UT, before exhibiting much larger variability that coincides with the presence of highly variable wave power for $0.1 < f/f_{ce} < 0.4$ during the period 01:50-02:30UT. Before 01:45UT, the wave power in the lowest frequency band appears independent of what is happening at other frequencies, whereas after 01:45UT, the wave power in the lowest frequency band seems to track the variability at higher frequencies. The correlation of wave power in different frequency bands will be explored in future works, but the interval displayed in Figure 5(a) suggests that high-variability waves in the lowest frequency band are connected to the high-variability chorus at higher frequencies.

8 Conclusions

Motivated by the aim of creating new spatio-temporal models of the diffusion coefficients that describe wave-particle interactions in the inner magnetosphere, we present occurrence rates and wave power statistics of whistler-mode wave activity in the region outside of the plasmasphere. Our principal findings are:

- The probability that an electron finds itself outside of the plasmasphere has a very different dependence on L^*, MLT and magnetic latitude from the probability that whistler-mode waves will be detected outside the plasmasphere. Both these probabilities are required to build a spatio-temporally varying model of diffusion coefficients.
- Occurrence rates of whistler-mode wave activity outside the plasmasphere are a strong function of MLT, magnetic latitude and frequency.
- Wave activity is almost always present with occurrence rates around 0.8 at relatively low frequencies in the whistler-mode range on the dayside of the inner magnetosphere, and this wave activity exhibits low variability during five-minute intervals.
- The occurrence rates of low-variability whistler-mode waves in the plasma-trough decrease with AE. The power of low-variability waves does not vary with AE.
- There is sporadic wave activity in the post-midnight, dawn and dayside sectors of the inner magnetosphere with overall occurrence rates around 0.2 with wave power that is highly-variable during five minute intervals.
- Occurrence rates of high-variability whistler-mode waves in the plasma-trough increase with increasing geomagnetic activity as defined by AE, as does wave power (up to a saturation level of around $AE \sim 350$ nT).

Interpreting the low-variability and high-variability whistler-mode waves in the context of previous work leads to the conclusion that low-variability waves are likely to be exohiss, whereas high-variability whistler-mode waves are traditional substorm-driven chorus. Some regions of the plasmatrough can support both high and low-variability waves in the same frequency bands. However, the dependence of high- and low-variability waves on AE indicates that they are driven in different ways.

One of the important factors highlighted in this work is that the two different types of whistler-mode waves found outside the plasmasphere not only have different frequencies and wave activity regions in (MLT, λ), but they also have different dependencies on geomagnetic activity, and different spatio-temporal characteristics. Our advance in distinguishing the different types of whistler-mode waves will enable improved statistical analyses of the behavior of both exohiss and substorm-driven chorus. Our results additionally allow for a more nuanced approach to modeling the whistler-mode wave electron interaction outside of the plasmasphere in the Earth's inner magnetosphere. The occurrence rates, variability in wave power, and driving factors that control each of the two types of waves are different. This means that diffusion coefficients for each type of whistler-mode wave in the plasmatrough should have very different statistical models. Building on previous numerical experiments (e.g. Watt et al., 2021), we suggest the next logical step is to run numerical Fokker-Planck experiments to determine the different response of the high-energy electron flux to persistent low variability exohiss versus highly-variable sporadic substorm-driven chorus.

9 Open Research

We acknowledge the NASA Van Allen probes and Craig Kletzing for use of the EMFISIS instrument data, available online (https://emfisis.physics.uiowa.edu/data/index). We also acknowledge the Radiation Belt Storm Probes ECT Science Operations and Data Center for the provision of the magnetic ephemeris data, available online (https://www.rbsp-ect.lanl.gov/data-pub/rbspa/MagEphem/). We thank Omniweb (https://omniweb.gsfc.nasa.gov/) for the provision of the AE indices used in this paper (Papitashvili & King, 2023). The wave power thresholds for electron cyclotron harmonic identification is archived at https://doi.org/10.25398/rd.northu

Acknowledgments

The research leading to these results has received funding from the Natural Environment Research Council (NERC) Grants NE/V00249X/1, NE/V002759/2 and NE/V002554/2 (Sat-Risk), alongside Science and Technology Facilities Council (STFC) Grant ST/X001008/1. NPM acknowledges support from NERC NE/X000389/1 and OA acknowledges the NERC Independent Research Fellowship NE/V013963/1 and NE/V013963/2.

References

Agapitov, O., Artemyev, A., Krasnoselskikh, V., Khotyaintsev, Y. V., Mourenas, D., Breuillard, H., ... Rolland, G. (2013). Statistics of whistler mode waves in the outer radiation belt: Cluster STAFF-SA measurements. *Journal of Geophysical Research: Space Physics*, *118*(6), 3407-3420. doi: 10.1002/jgra.50312

Agapitov, O., Blum, L. W., Mozer, F. S., Bonnell, J. W., & Wygant, J. (2017). Chorus whistler wave source scales as determined from multipoint Van Allen Probe measurements. *Geophysical Research Letters*, *44*(6), 2634-2642. doi: https://doi.org/10.1002/2017GL072701

Agapitov, O., Krasnoselskikh, V., Khotyaintsev, Y. V., & Rolland, G. (2011). A statistical study of the propagation characteristics of whistler waves observed by Cluster. *Geophysical Research Letters*, *38*(20). doi: https://doi.org/10.1029/2011GL049597

Agapitov, O., Mourenas, D., Artemyev, A., Mozer, F. S., Bonnell, J. W., Angelopoulos, V., ... Krasnoselskikh, V. (2018). Spatial extent and temporal correlation of chorus and hiss: Statistical results from multipoint THEMIS observations. *Journal of Geophysical Research: Space Physics*, *123*(10), 8317-8330. doi: 10.1029/2018JA025725

Allanson, O., Elsden, T., Watt, C., & Neukirch, T. (2022). Weak turbulence and quasilinear diffusion for relativistic wave-particle interactions via a Markov approach. *Frontiers in Astronomy and Space Sciences*, *8*. doi: 10.3389/fspas.2021.805699

Allcock, G. M. (1957). A study of the audio-frequency radio phenomenon known as "Dawn Chorus". *Australian Journal of Physics*, *10*, 286–298.

Allison, H. J., Shprits, Y. Y., Zhelavskaya, I. S., Wang, D., & Smirnov, A. G. (2021). Gyroresonant wave-particle interactions with chorus waves during extreme depletions of plasma density in the Van Allen radiation belts. *Science Advances*, *7*(5), eabc0380. doi: 10.1126/sciadv.abc0380

Artemyev, A., Agapitov, O., Mourenas, D., Krasnoselskikh, V., Shastun, V., & Mozer, F. (2016). Oblique whistler-mode waves in the earth's inner magnetosphere: Energy distribution, origins, and role in radiation belt dynamics. *Space Science Reviews*, *200*, 261–355. doi: 10.1007/s11214-016-0252-5

Aryan, H., Sibeck, D., Balikhin, M., Agapitov, O., & Kletzing, C. (2016). Observation of chorus waves by the Van Allen Probes: Dependence on solar wind parameters and scale size. *Journal of Geophysical Research: Space Physics*, *121*(8), 7608-7621. doi: 10.1002/2016JA022775

Aryan, H., Yearby, K., Balikhin, M., Agapitov, O., Krasnoselskikh, V., & Boynton, R. (2014). Statistical study of chorus wave distributions in the inner magnetosphere using AE and solar wind parameters. *Journal of Geophysical Research: Space Physics*, *119*(8), 6131-6144. doi: https://doi.org/10.1002/2014JA019939

Bentley, S. N., Watt, C. E. J., Rae, I. J., Owens, M. J., Murphy, K., Lockwood, M., & Sandhu, J. K. (2019). Capturing uncertainty in magnetospheric ultralow frequency wave models. *Space Weather*, *17*(4), 599-618. doi: https://doi.org/10.1029/2018SW002102

Bortnik, J., Thorne, R. M., & Meredith, N. P. (2007). Modeling the propagation characteristics of chorus using CRRES suprathermal electron fluxes. *Journal of*

Geophysical Research: Space Physics, *112*(A8). doi: https://doi.org/10.1029/2006JA012237

Bourdarie, S., Boscher, D., Beutier, T., Sauvaud, J., & Blanc, M. (1997). Physical modeling of radiation belt response to geomagnetic storm: 2. On a 10 hour–10 day time scale. *Advances in Space Research*, *20*(3), 381-384. Retrieved from `https://www.sciencedirect.com/science/article/pii/S0273117797006960` (The Subauroral Ionosphere, Plasmasphere, Ring Current and Inner Magnetosphere System) doi: https://doi.org/10.1016/S0273-1177(97)00696-0

Cattell, C., Wygant, J. R., Goetz, K., Kersten, K., Kellogg, P. J., von Rosenvinge, T., ... Russell, C. T. (2008). Discovery of very large amplitude whistler-mode waves in earth's radiation belts. *Geophysical Research Letters*, *35*(1). doi: https://doi.org/10.1029/2007GL032009

Chakraborty, S., & Morley, S. K. (2020). Probabilistic prediction of geomagnetic storms and the kp index. *J. Space Weather Space Clim.*, *10*, 36. doi: 10.1051/swsc/2020037

Chan, A. A., Elkington, S. R., Longley, W. J., Aldhurais, S. A., Alam, S. S., Albert, J. M., ... Li, W. (2023). Simulation of radiation belt wave-particle interactions in an MHD-particle framework. *Frontiers in Astronomy and Space Sciences*, *10*. doi: 10.3389/fspas.2023.1239160

Cully, C. M., Angelopoulos, V., Auster, U., Bonnell, J., & Le Contel, O. (2011). Observational evidence of the generation mechanism for rising-tone chorus. *Geophysical Research Letters*, *38*(1). doi: https://doi.org/10.1029/2010GL045793

Cunningham, G. S. (2023). Resolution of a few problems in the application of quasi-linear theory to calculating diffusion coefficients in heliophysics. *Journal of Geophysical Research: Space Physics*, *128*(10), e2023JA031703. doi: https://doi.org/10.1029/2023JA031703

Daggitt, T., Horne, R., Glauert, S., Del Zanna, G., & Albert, J. M. (2024). Chorus wave power at the strong diffusion limit overcomes electron losses due to strong diffusion. *Nature Communications*, *15*. doi: 10.1038/s41467-024-45967-9

Drozdov, A. Y., Shprits, Y. Y., Orlova, K. G., Kellerman, A. C., Subbotin, D. A., Baker, D. N., ... Reeves, G. D. (2015). Energetic, relativistic, and ultrarelativistic electrons: Comparison of long-term VERB code simulations with Van Allen Probes measurements. *Journal of Geophysical Research: Space Physics*, *120*(5), 3574-3587. doi: 10.1002/2014JA020637

Ebihara, Y., & Miyoshi, Y. (2011). Dynamic inner magnetosphere: A tutorial and recent advances. In *Iaga special sopron book series vol. 3* (pp. 145–187).

Feng, B., Li, H., Yu, X., Yuan, Z., Tang, R., Wang, D., ... Deng, X. (2023). The evolution of whistler hiss-like waves across plasmapause: Hiss to exohiss. *Geophysical Research Letters*, *50*(8), e2023GL102993. doi: https://doi.org/10.1029/2023GL102993

Fiori, R. A. D., Trichtchenko, L., Balch, C., Spanswick, E., & Groleau, S. (2020). Characterizing auroral-zone absorption based on global kp and regional geomagnetic hourly range indices. *Space Weather*, *18*(12), e2020SW002572. doi: https://doi.org/10.1029/2020SW002572

Gao, Z., Su, Z., Xiao, F., Zheng, H., Wang, Y., Wang, S., ... Funsten, H. O. (2018). Exohiss wave enhancement following substorm electron injection in the dayside magnetosphere. *Earth and Planetary Physics*, *2*(5), 359-370.

Glauert, S. A., & Horne, R. B. (2005). Calculation of pitch angle and energy diffusion coefficients with the PADIE code. *Journal of Geophysical Research: Space Physics*, *110*(A4). doi: 10.1029/2004JA010851

Glauert, S. A., Horne, R. B., & Meredith, N. P. (2014a). Simulating the Earth's radiation belts: Internal acceleration and continuous losses to the magnetopause. *Journal of Geophysical Research: Space Physics*, *119*(9), 7444-7463. doi: 10.1002/2014JA020092

Glauert, S. A., Horne, R. B., & Meredith, N. P. (2014b). Three-dimensional electron radiation belt simulations using the BAS Radiation Belt Model with new diffusion models for chorus, plasmaspheric hiss, and lightning-generated whistlers. *Journal of Geophysical Research: Space Physics*, *119*(1), 268-289. doi: 10.1002/2013JA019281

Glauert, S. A., Horne, R. B., & Meredith, N. P. (2018). A 30-year simulation of the outer electron radiation belt. *Space Weather*, *0*(0). doi: 10.1029/2018SW001981

Goldstein, J. (2006). Plasmasphere response: Tutorial and review of recent imaging results. *Space Science Reviews*, *124*, 203-216. doi: 10.1007/s11214-006-9105-y

Green, J. C., & Kivelson, M. G. (2004). Relativistic electrons in the outer radiation belt: Differentiating between acceleration mechanisms. *Journal of Geophysical Research: Space Physics*, *109*(A3). doi: https://doi.org/10.1029/2003JA010153

Hanzelka, M., & Santolík. (2024). Theories of growth and propagation of parallel whistler-mode chorus emissions: A review. *Surveys in Geophysics*, *45*, 1–54. doi: https://doi.org/10.1007/s10712-023-09792-x

Hartley, D. P., Chen, L., Christopher, I. W., Kletzing, C. A., Santolik, O., Li, W., & Shi, R. (2022). The angular distribution of lower band chorus waves near plasmaspheric plumes. *Geophysical Research Letters*, *49*(9), e2022GL098710. doi: https://doi.org/10.1029/2022GL098710

Helliwell, R. A. (1969). Low-frequency waves in the magnetosphere. *Reviews of Geophysics*, *7*(1-2), 281-303. doi: https://doi.org/10.1029/RG007i001p00281

Horne, R. B., Glauert, S. A., & Thorne, R. M. (2003b). Resonant diffusion of radiation belt electrons by whistler-mode chorus. *Geophysical Research Letters*, *30*, 1493–1496.

Horne, R. B., Kersten, T., Glauert, S. A., Meredith, N. P., Boscher, D., Sicard-Piet, A., ... Li, W. (2013). A new diffusion matrix for whistler mode chorus waves. *Journal of Geophysical Research: Space Physics*, *118*(10), 6302-6318. doi: 10.1002/jgra.50594

Horne, R. B., Meredith, N. M., Glauert, S. A., & Kersten, T. (2016). Wave driven diffusion in radiation belt dynamics. In G. Balasis, I. A. Daglis, & I. R. Mann (Eds.), *Waves, particles, and storms in geospace: a complex interplay* (p. 217-243). Oxford: Oxford University Press.

Horne, R. B., Thorne, R. M., Glauert, S. A., Albert, J. M., Meredith, N. P., & Anderson, R. R. (2005a). Timescale for radiation belt electron acceleration by whistler mode chorus waves. *Journal of Geophysical Research: Space Physics*, *110*(A3). doi: 10.1029/2004JA010811

Horne, R. B., Thorne, R. M., Shprits, Y. Y., Meredith, N. M., Glauert, S. A., Smith, A. J., ... Decreau, P. M. E. (2005b). Wave acceleration of electrons in the Van Allen radiation belts. *Nature*, *437*. doi: 10.1038/nature03939

Hospodarsky, G. B., Averkamp, T. F., Kurth, W. S., Gurnett, D. A., Dougherty, M., Inan, U., & Wood, T. (2001). Wave normal and poynting vector calculations using the cassini radio and plasma wave instrument. *Journal of Geophysical Research: Space Physics*, *106*(A12), 30253-30269. doi: https://doi.org/10.1029/2001JA900114

Iles, R. H. A., Meredith, N. P., Fazakerley, A. N., & Horne, R. B. (2006). Phase space density analysis of the outer radiation belt energetic electron dynamics. *Journal of Geophysical Research: Space Physics*, *111*(A3). doi: https://doi.org/10.1029/2005JA011206

Jin, Y., Liu, N., Su, Z., Zheng, H., Wang, Y., & Wang, S. (2022). Immediate impact of solar wind dynamic pressure pulses on whistler-mode chorus waves in the inner magnetosphere. *Geophysical Research Letters*, *49*(5), e2022GL097941. doi: https://doi.org/10.1029/2022GL097941

Kennel, C. F., & Engelmann, F. (1966, December). Velocity Space Diffusion from Weak Plasma Turbulence in a Magnetic Field. *Physics of Fluids*, *9*, 2377-2388.

doi: 10.1063/1.1761629

Kletzing, C. A., Bortnik, J., Hospodarsky, G., Kurth, W. S., Santolik, O., Smith, C. W., ... Gupta, A. S. (2023). The Electric and Magnetic Fields Instrument Suite and Integrated Science (EMFISIS): Science, Data, and Usage Best Practices. *Space Science Reviews*, *219*(28). doi: https://doi.org/10.1007/s11214-023-00973-z

Kletzing, C. A., Kurth, W. S., Acuna, M., MacDowall, R. J., Torbert, R. B., Averkamp, T., ... Tyler, J. (2013, Nov 01). The Electric and Magnetic Field Instrument Suite and Integrated Science (EMFISIS) on RBSP. *Space Science Reviews*, *179*(1), 127–181. doi: 10.1007/s11214-013-9993-6

Kurth, W. S., De Pascuale, S., Faden, J. B., Kletzing, C. A., Hospodarsky, G. B., Thaller, S., & Wygant, J. R. (2015). Electron densities inferred from plasma wave spectra obtained by the Waves instrument on Van Allen Probes. *Journal of Geophysical Research: Space Physics*, *120*(2), 904-914. doi: 10.1002/2014JA020857

LeDocq, M. J., Gurnett, D. A., & Hospodarsky, G. B. (1998). Chorus source locations from VLF Poynting flux measurements with the Polar spacecraft. *Geophysical Research Letters*, *25*(21), 4063-4066. doi: https://doi.org/10.1029/1998GL900071

Lejosne, S., Allison, H. J., Blum, L. W., Drozdov, A. Y., Hartinger, M. D., Hudson, M. K., ... Zhao, H. (2022). Differentiating between the leading processes for electron radiation belt acceleration. *Frontiers in Astronomy and Space Sciences*, *9*.

Lemons, D. S. (2012). Pitch angle scattering of relativistic electrons from stationary magnetic waves: Continuous Markov process and quasilinear theory. *Physics of Plasmas*, *19*, 012306.

Li, J., Bortnik, J., An, X., Li, W., Angelopoulos, V., Thorne, R. M., ... Baker, D. B. (2019). Origin of two-band chorus in the radiation belt of Earth. *Nature Communications*, *10*, 1. doi: 10.1038/s41467-019-12561-3

Li, W., Bortnik, J., Thorne, R. M., Cully, C. M., Chen, L., Angelopoulos, V., ... LeContel, O. (2013). Characteristics of the poynting flux and wave normal vectors of whistler-mode waves observed on THEMIS. *Journal of Geophysical Research: Space Physics*, *118*(4), 1461-1471. doi: https://doi.org/10.1002/jgra.50176

Li, W., & Hudson, M. (2019). Earth's Van Allen Radiation Belts: From Discovery to the Van Allen Probes Era. *Journal of Geophysical Research: Space Physics*, *124*(11), 8319-8351. doi: https://doi.org/10.1029/2018JA025940

Li, W., Ma, Q., Thorne, R. M., Bortnik, J., Kletzing, C. A., Kurth, W. S., ... Nishimura, Y. (2015). Statistical properties of plasmaspheric hiss derived from Van Allen Probes data and their effects on radiation belt electron dynamics. *Journal of Geophysical Research: Space Physics*, *120*(5), 3393-3405. doi: 10.1002/2015JA021048

Li, W., Santolik, O., Bortnik, J., Thorne, R. M., Kletzing, C. A., Kurth, W. S., & Hospodarsky, G. B. (2016). New chorus wave properties near the equator from Van Allen Probes wave observations. *Geophysical Research Letters*, *43*(10), 4725-4735. doi: 10.1002/2016GL068780

Li, W., Thorne, R. M., Angelopoulos, V., Bortnik, J., Cully, C. M., Ni, B., ... Magnes, W. (2009). Global distribution of whistler-mode chorus waves observed on the THEMIS spacecraft. *Geophysical Research Letters*, *36*(9). doi: https://doi.org/10.1029/2009GL037595

Li, W., Thorne, R. M., Bortnik, J., Shprits, Y. Y., Nishimura, Y., Angelopoulos, V., ... Bonnell, J. W. (2011). Typical properties of rising and falling tone chorus waves. *Geophysical Research Letters*, *38*(14). doi: https://doi.org/10.1029/2011GL047925

Li, W., Thorne, R. M., Bortnik, J., Tao, X., & Angelopoulos, V. (2012). Characteristics of hiss-like and discrete whistler-mode emissions. *Geophysical Research Let-*

ters, *39*(18). doi: 10.1029/2012GL053206

Li, W., Thorne, R. M., Nishimura, Y., Bortnik, J., Angelopoulos, V., McFadden, J. P., ... Auster, U. (2010). THEMIS analysis of observed equatorial electron distributions responsible for the chorus excitation. *Journal of Geophysical Research: Space Physics*, *115*(A6). doi: https://doi.org/10.1029/2009JA014845

Liu, N., & Su, Z. (2023). Prompt responses of magnetospheric whistler-mode waves to solar wind dynamic pressure pulses. *Frontiers in Astronomy and Space Sciences*, *10*. doi: https://doi.org/10.3389/fspas.2023.1193600

Lyons, L. R., Thorne, R. M., & Kennel, C. F. (1972). Pitch-angle diffusion of radiation belt electrons within the plasmasphere. *Journal of Geophysical Research*, *77*(19), 3455-3474. doi: 10.1029/JA077i019p03455

Ma, Q., Chu, X., Ma, D., Huang, S., Li, W., Bortnik, J., & Shen, X.-C. (2023). Evaluating the performance of empirical models of total electron density and whistler-mode wave amplitude in the earth's inner magnetosphere. *Frontiers in Astronomy and Space Sciences*, *10*. doi: 10.3389/fspas.2023.1232702

Malaspina, D. M., Jaynes, A. N., Hospodarsky, G., Bortnik, J., Ergun, R. E., & Wygant, J. (2017). Statistical properties of low-frequency plasmaspheric hiss. *Journal of Geophysical Research: Space Physics*, *122*(8), 8340-8352. doi: 10.1002/2017JA024328

Malaspina, D. M., Zhu, H., & Drozdov, A. Y. (2020). A wave model and diffusion coefficients for plasmaspheric hiss parameterized by plasmapause location. *Journal of Geophysical Research: Space Physics*, *125*(2), e2019JA027415. doi: https://doi.org/10.1029/2019JA027415

Meredith, N. P., Horne, R. B., & Anderson, R. R. (2001). Substorm dependence of chorus amplitudes: Implications for the acceleration of electrons to relativistic energies. *Journal of Geophysical Research: Space Physics*, *106*(A7), 13165-13178. doi: 10.1029/2000JA900156

Meredith, N. P., Horne, R. B., Glauert, S. A., & Anderson, R. R. (2007). Slot region electron loss timescales due to plasmaspheric hiss and lightning-generated whistlers. *Journal of Geophysical Research: Space Physics*, *112*(A8). doi: 10.1029/2007JA012413

Meredith, N. P., Horne, R. B., Glauert, S. A., Baker, D. N., Kanekal, S. G., & Albert, J. M. (2009). Relativistic electron loss timescales in the slot region. *Journal of Geophysical Research: Space Physics*, *114*(A3). doi: 10.1029/2008JA013889

Meredith, N. P., Horne, R. B., Glauert, S. A., Thorne, R. M., Summers, D., Albert, J. M., & Anderson, R. R. (2006). Energetic outer zone electron loss timescales during low geomagnetic activity. *Journal of Geophysical Research: Space Physics*, *111*(A05212). doi: 10.1029/2005JA011516

Meredith, N. P., Horne, R. B., Kersten, T., Li, W., Bortnik, J., Sicard, A., & Yearby, K. H. (2018). Global model of plasmaspheric hiss from multiple satellite observations. *Journal of Geophysical Research: Space Physics*, *123*(6), 4526-4541. doi: 10.1029/2018JA025226

Meredith, N. P., Horne, R. B., Li, W., Thorne, R. M., & Sicard-Piet, A. (2014). Global model of low-frequency chorus ($f_{LHR} < f < 0.1f_{ce}$) from multiple satellite observations. *Geophysical Research Letters*, *41*(2), 280-286.

Meredith, N. P., Horne, R. B., Shen, X.-C., Li, W., & Bortnik, J. (2020). Global model of whistler mode chorus in the near-equatorial region ($\|\lambda_m\| < 18°$). *Geophysical Research Letters*, *47*(11), e2020GL087311. doi: 10.1029/2020GL087311

Meredith, N. P., Horne, R. B., Sicard-Piet, A., Boscher, D., Yearby, K. H., Li, W., & Thorne, R. M. (2012). Global model of lower band and upper band chorus from multiple satellite observations. *Journal of Geophysical Research: Space Physics*, *117*(A10). doi: https://doi.org/10.1029/2012JA017978

Meredith, N. P., Horne, R. B., Thorne, R. M., Summers, D., & Anderson, R. R. (2004). Substorm dependence of plasmaspheric hiss. *Journal of Geophysical*

Research: Space Physics, *109*(A6). doi: 10.1029/2004JA010387

Mourenas, D., Artemyev, A. V., Agapitov, O. V., & Krasnoselskikh, V. (2014). Consequences of geomagnetic activity on energization and loss of radiation belt electrons by oblique chorus waves. *Journal of Geophysical Research: Space Physics*, *119*(4), 2775-2796. doi: https://doi.org/10.1002/2013JA019674

Murphy, K. R., Mann, I. R., Rae, I. J., Sibeck, D. G., & Watt, C. E. J. (2016). Accurately characterizing the importance of wave-particle interactions in radiation belt dynamics: The pitfalls of statistical wave representations. *Journal of Geophysical Research: Space Physics*, *121*(8), 7895-7899. doi: https://doi.org/10.1002/2016JA022618

Muto, H., & Hayakawa, M. (1987). Ray-tracing study of the propagation in the magnetosphere of whistler-mode VLF emissions with frequency above one half the gyrofrequency. *Planetary and Space Science*, *35*(11), 1397-1404. doi: https://doi.org/10.1016/0032-0633(87)90052-3

Muto, H., Hayakawa, M., Parrot, M., & Lefeuvre, F. (1987). Direction finding of half-gyrofrequency VLF emissions in the off-equatorial region of the magnetosphere and their generation and propagation. *Journal of Geophysical Research: Space Physics*, *92*(A7), 7538-7550. doi: https://doi.org/10.1029/JA092iA07p07538

Nagano, I., Yagitani, S., Kojima, H., & Matsumoto, H. (1996). Analysis of wave normal and poynting vectors of the chorus emissions observed by GEOTAIL. *Journal of geomagnetism and geoelectricity*, *48*(3), 299-307. doi: 10.5636/jgg.48.299

Ni, B., Bortnik, J., Thorne, R. M., Ma, Q., & Chen, L. (2013). Resonant scattering and resultant pitch angle evolution of relativistic electrons by plasmaspheric hiss. *Journal of Geophysical Research: Space Physics*, *118*(12), 7740-7751. doi: 10.1002/2013JA019260

Ni, B., Li, W., Thorne, R. M., Bortnik, J., Ma, Q., Chen, L., ... Claudepierre, S. G. (2014). Resonant scattering of energetic electrons by unusual low-frequency hiss. *Geophysical Research Letters*, *41*(6), 1854-1861. doi: 10.1002/2014GL059389

Omura, Y. (2021). Nonlinear wave growth theory of whistler-mode chorus and hiss emissions in the magnetosphere. *Earth Planets Space*, *73*. doi: 10.1186/s40623-021-01380-w

Papitashvili, N. E., & King, J. H. (2023). *OMNI 1-min data [data set].* `https://doi.org/10.48322/45bb-8792`. doi: 10.48322/45bb-8792

Reeves, G. D., Spence, H. E., Henderson, M. G., Morley, S. K., Friedel, R. H. W., Funsten, H. O., ... Niehof, J. T. (2013). Electron acceleration in the heart of the Van Allen radiation belts. *Science*, *1095-9203*, 991–4. doi: 10.1126/science.1237743

Ripoll, J.-F., Albert, J. M., & Cunningham, G. S. (2014). Electron lifetimes from narrowband wave-particle interactions within the plasmasphere. *Journal of Geophysical Research: Space Physics*, *119*(11), 8858-8880. doi: https://doi.org/10.1002/2014JA020217

Ripoll, J.-F., Claudepierre, S. G., Ukhorskiy, A. Y., Colpitts, C., Li, X., Fennell, J. F., & Crabtree, C. (2020). Particle dynamics in the Earth's radiation belts: Review of current research and open questions. *Journal of Geophysical Research: Space Physics*, *125*(5), e2019JA026735. doi: 10.1029/2019JA026735

Ripoll, J.-F., Santolík, O., Reeves, G. D., Kurth, W. S., Denton, M. H., Loridan, V., ... Turner, D. L. (2017). Effects of whistler mode hiss waves in March 2013. *Journal of Geophysical Research: Space Physics*, *122*(7), 7433-7462. doi: 10.1002/2017JA024139

Ripoll, J.-F., Thaller, S. A., Hartley, D. P., Malaspina, D. M., Kurth, W. S., Cunningham, G. S., ... Wygant, J. (2024). Statistics and models of the electron plasma density from the van allen probes. *Journal of Geophysical Research: Space Physics*, *129*(8), e2024JA032528. doi: https://doi.org/10.1029/2024JA032528

Rodger, C. J., Cresswell-Moorcock, K., & Clilverd, M. A. (2016). Nature's Grand Experiment: Linkage between magnetospheric convection and the radiation belts. *Journal of Geophysical Research: Space Physics*, *121*(1), 171-189. doi: https://doi.org/10.1002/2015JA021537

Ross, J. P. J., Glauert, S. A., Horne, R. B., Watt, C. E. J., Meredith, N. P., & Woodfield, E. E. (2020). A new approach to constructing models of electron diffusion by EMIC waves in the radiation belts. *Geophysical Research Letters*, *n/a*(n/a), e2020GL088976. doi: 10.1029/2020GL088976

Santolík, O., Gurnett, D. A., Pickett, J. S., Grimald, S., Décreau, P. M. E., Parrot, M., ... Fazakerley, A. (2010). Wave-particle interactions in the equatorial source region of whistler-mode emissions. *Journal of Geophysical Research: Space Physics*, *115*(A8). doi: https://doi.org/10.1029/2009JA015218

Santolík, O., Macúšová, E., Kolmašová, I., Cornilleau-Wehrlin, N., & de Conchy, Y. (2014). Propagation of lower-band whistler-mode waves in the outer Van Allen belt: Systematic analysis of 11 years of multi-component data from the Cluster spacecraft. *Geophysical Research Letters*, *41*(8), 2729-2737. doi: https://doi.org/10.1002/2014GL059815

Seo, J., & Kim, K.-C. (2023). The relationship of exohiss waves with plasmaspheric hiss distribution and solar wind parameters. *Journal of Geophysical Research: Space Physics*, *128*(10), e2023JA031777. doi: https://doi.org/10.1029/2023JA031777

Spasojevic, M., & Inan, U. S. (2010). Drivers of chorus in the outer dayside magnetosphere. *Journal of Geophysical Research: Space Physics*, *115*(A4). doi: https://doi.org/10.1029/2009JA014452

Spasojevic, M., Shprits, Y. Y., & Orlova, K. (2015). Global empirical models of plasmaspheric hiss using Van Allen Probes. *Journal of Geophysical Research: Space Physics*, *120*(12), 10,370-10,383. doi: 10.1002/2015JA021803

Tang, R., Yuan, A., Li, H., Ouyang, Z., & Deng, X. (2023). Influence of solar wind dynamic pressure on distribution of whistler mode waves based on Van Allen Probe observations. *Journal of Geophysical Research: Space Physics*, *128*(4), e2022JA031181. doi: https://doi.org/10.1029/2022JA031181

Tao, X., Zonca, F., & Chen, L. (2021). A "Trap-Release-Amplify" model of chorus waves. *Journal of Geophysical Research: Space Physics*, *126*(9), e2021JA029585. doi: https://doi.org/10.1029/2021JA029585

Taubenschuss, U., Khotyaintsev, Y. V., Santolík, O., Vaivads, A., Cully, C. M., Contel, O. L., & Angelopoulos, V. (2014). Wave normal angles of whistler mode chorus rising and falling tones. *Journal of Geophysical Research: Space Physics*, *119*(12), 9567-9578. doi: https://doi.org/10.1002/2014JA020575

Tebaldi, C., & Knutti, R. (2007). The use of the multi-model ensemble in probabilistic climate projections. *Philosophical Transactions of the Royal Society A*, *365*, 2053—2075. doi: 10.1098/rsta.2007.2076

Thompson, R. L., Watt, C. E. J., & Williams, P. D. (2020). Accounting for variability in ULF wave radial diffusion models. *Journal of Geophysical Research: Space Physics*, *125*(8), e2019JA027254. doi: 10.1029/2019JA027254

Thorne, R. M. (2010). Radiation belt dynamics: The importance of wave-particle interactions. *Geophysical Research Letters*, *37*(22). doi: 10.1029/2010GL044990

Thorne, R. M., Smith, E. J., Burton, R. K., & Holzer, R. E. (1973). Plasmaspheric hiss. *Journal of Geophysical Research*, *78*(10), 1581-1596. doi: 10.1029/JA078i010p01581

Tsyganenko, N. A., & Sitnov, M. I. (2005). Modeling the dynamics of the inner magnetosphere during strong geomagnetic storms. *Journal of Geophysical Research: Space Physics*, *110*(A3). doi: https://doi.org/10.1029/2004JA010798

Tu, W., Cunningham, G. S., Chen, Y., Henderson, M. G., Camporeale, E., & Reeves, G. D. (2013). Modeling radiation belt electron dynamics during GEM

challenge intervals with the DREAM3D diffusion model. *Journal of Geophysical Research: Space Physics*, *118*(10), 6197-6211. doi: 10.1002/jgra.50560

Tyler, E., Breneman, A., Cattell, C., Wygant, J., Thaller, S., & Malaspina, D. (2019). Statistical distribution of whistler mode waves in the radiation belts with large magnetic field amplitudes and comparison to large electric field amplitudes. *Journal of Geophysical Research: Space Physics*, *124*(8), 6541 – 6552. doi: 10.1029/2019JA026913

Wang, D., & Shprits, Y. Y. (2019). On how high-latitude chorus waves tip the balance between acceleration and loss of relativistic electrons. *Geophysical Research Letters*, *46*(14), 7945-7954. doi: https://doi.org/10.1029/2019GL082681

Wang, D., Shprits, Y. Y., Zhelavskaya, I. S., Agapitov, O. V., Drozdov, A. Y., & Aseev, N. A. (2019). Analytical chorus wave model derived from Van Allen Probe observations. *Journal of Geophysical Research: Space Physics*, *124*(2), 1063-1084. doi: 10.1029/2018JA026183

Wang, J. L., Li, L. Y., & Yu, J. (2020). Statistical relationship between exohiss waves and plasmaspheric hiss. *Geophysical Research Letters*, *47*(5), e2020GL087023. doi: https://doi.org/10.1029/2020GL087023

Watt, C. E. J., Allison, H. J., Bentley, S. N., Thompson, R. L., Rae, I. J., Allanson, O., ... Killey, S. (2022). Temporal variability of quasi-linear pitch-angle diffusion. *Frontiers in Astronomy and Space Sciences*, *9*. doi: 10.3389/fspas.2022.1004634

Watt, C. E. J., Allison, H. J., Meredith, N. P., Thompson, R. L., Bentley, S. N., Rae, I. J., ... Horne, R. B. (2019). Variability of Quasilinear Diffusion Coefficients for Plasmaspheric Hiss. *Journal of Geophysical Research: Space Physics*, *124*(10), 9545-9551. doi: 10.1002/2018JA026401

Watt, C. E. J., Allison, H. J., Thompson, R. L., Bentley, S. N., Meredith, N. P., Glauert, S. A., ... Rae, I. J. (2021). The implications of temporal variability in wave-particle interactions in Earth's radiation belts. *Geophysical Research Letters*, *48*(1), e2020GL089962. doi: https://doi.org/10.1029/2020GL089962

Watt, C. E. J., Degeling, A. W., & Rankin, R. (2013). Constructing the frequency and wave normal distribution of whistler-mode wave power. *Journal of Geophysical Research: Space Physics*, *118*(5), 1984-1991. doi: https://doi.org/10.1002/jgra.50231

Watt, C. E. J., Rae, I. J., Murphy, K. R., Anekallu, C., Bentley, S. N., & Forsyth, C. (2017). The parameterization of wave-particle interactions in the Outer Radiation Belt. *Journal of Geophysical Research: Space Physics*, *122*(9), 9545-9551. doi: 10.1002/2017JA024339

Watt, C. E. J., Rankin, R., & Degeling, A. W. (2012). Whistler mode wave growth and propagation in the prenoon magnetosphere. *Journal of Geophysical Research: Space Physics*, *117*(A6). doi: https://doi.org/10.1029/2012JA017765

Wilson III, L. B., Cattell, C. A., Kellogg, P. J., Wygant, J. R., Goetz, K., Breneman, A., & Kersten, K. (2011). The properties of large amplitude whistler mode waves in the magnetosphere: Propagation and relationship with geomagnetic activity. *Geophysical Research Letters*, *38*(17). doi: https://doi.org/10.1029/2011GL048671

Wong, J.-M., Meredith, N. P., Horne, R. B., Glauert, S. A., & Ross, J. P. J. (2022). Electron diffusion by magnetosonic waves in the Earth's radiation belts. *Journal of Geophysical Research: Space Physics*, *127*(4), e2021JA030196. doi: https://doi.org/10.1029/2021JA030196

Wong, J.-M., Meredith, N. P., Horne, R. B., Glauert, S. A., & Ross, J. P. J. (2024). New chorus diffusion coefficients for radiation belt modeling. *Journal of Geophysical Research: Space Physics*, *129*(1), e2023JA031607. doi: https://doi.org/10.1029/2023JA031607

Zhang, S., Rae, I. J., Watt, C. E. J., Degeling, A. W., Tian, A., Shi, Q., ... Wang, H. (2021). Determining the global scale size of chorus waves in the magneto-

sphere. *Journal of Geophysical Research: Space Physics*, *126*(11), e2021JA029569. doi: https://doi.org/10.1029/2021JA029569

Zhang, X.-J., Demekhov, A. G., Katoh, Y., Nunn, D., Tao, X., Mourenas, D., ... Angelopoulos, V. (2021). Fine structure of chorus wave packets: Comparison between observations and wave generation models. *Journal of Geophysical Research: Space Physics*, *126*(8), e2021JA029330. doi: https://doi.org/10.1029/2021JA029330

Zhou, Q., Li, J., Xiao, F., Zhang, S., Liu, S., Yang, C., ... Gao, Z. (2023). Global occurrence of higher-bands ech waves in radiation belts based on a novel noise reduction algorithm (nora). *Geophysical Research Letters*, *50*(6), e2022GL101889. doi: https://doi.org/10.1029/2022GL101889

Zhu, H., Gu, W., & Chen, L. (2019). Statistical analysis on plasmatrough exohiss waves from the Van Allen Probes. *Journal of Geophysical Research: Space Physics*, *124*(6), 4356-4364. doi: https://doi.org/10.1029/2018JA026359

Zhu, H., Su, Z., Xiao, F., Zheng, H., Wang, Y., Shen, C., ... Baker, D. N. (2015). Plasmatrough exohiss waves observed by Van Allen Probes: Evidence for leakage from plasmasphere and resonant scattering of radiation belt electrons. *Geophysical Research Letters*, *42*(4), 1012-1019. doi: https://doi.org/10.1002/2014GL062964

Figure 1.

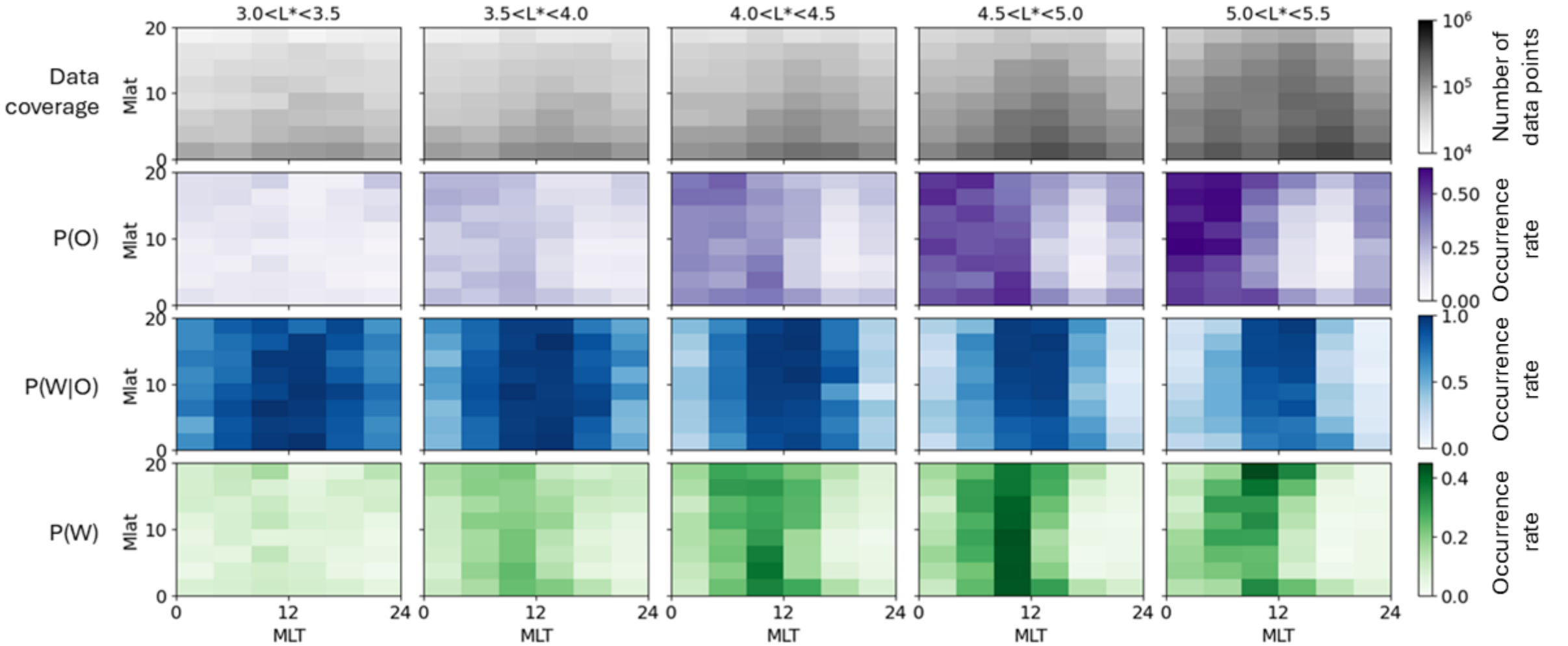
3.0<L*<3.5
3.5<L*<4.0
4.0<L*<4.5
4.5<L*<5.5
5.0<L*<5.5
Data coverage
P(O)
P(W|O)
P(W)
Mlat
MLT
0
12
24
20
10
Number of data points
10^6
10^5
10^4
Occurrence rate
0.50
0.25
0.00
1.0
0.5
0.0
0.4
0.2

Figure 2.

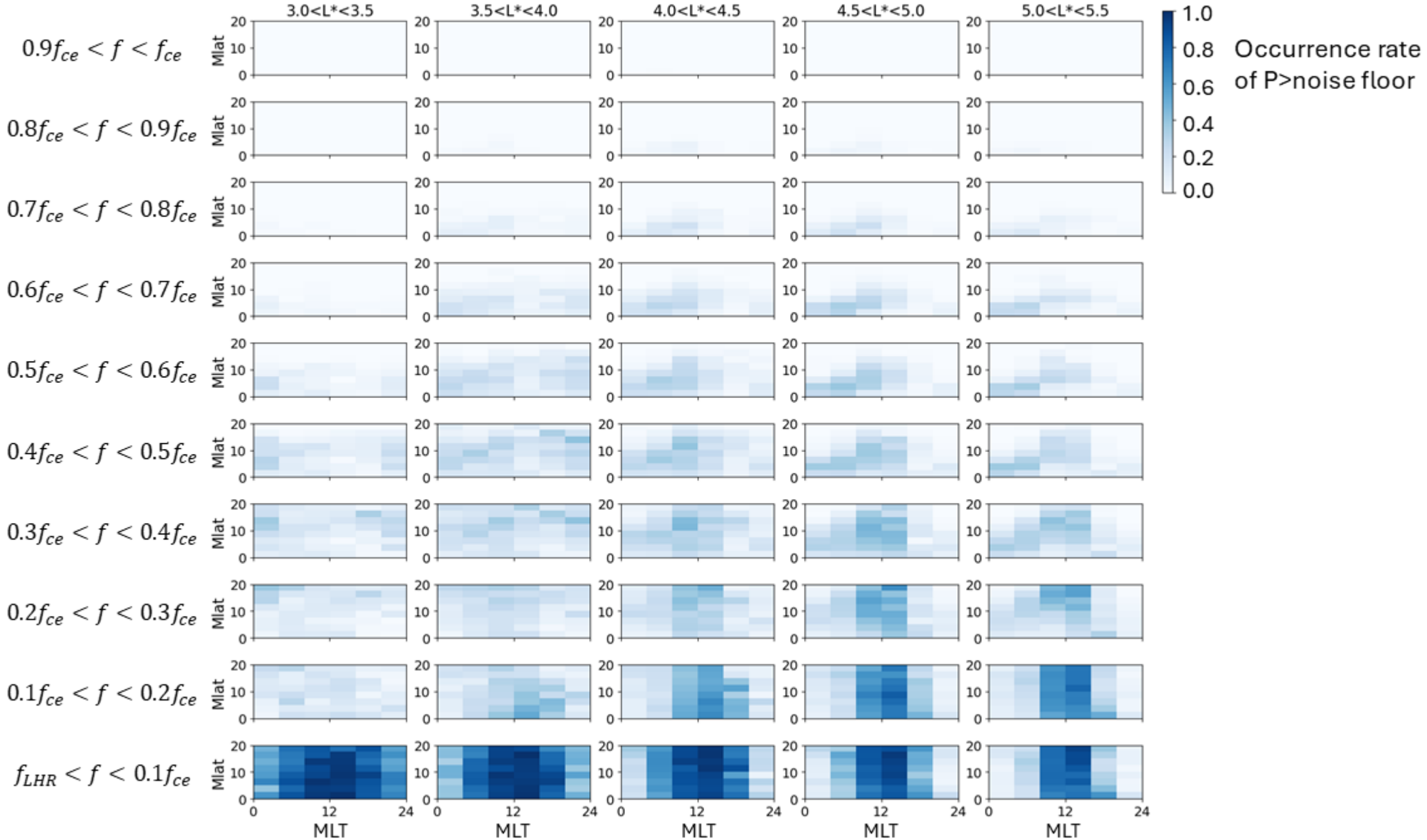
3.0<L*<3.5
3.5<L*<4.0
4.0<L*<4.5
4.5<L*<5.0
5.0<L*<5.5
$0.9f_{ce} < f < f_{ce}$
$0.8f_{ce} < f < 0.9f_{ce}$
$0.7f_{ce} < f < 0.8f_{ce}$
$0.6f_{ce} < f < 0.7f_{ce}$
$0.5f_{ce} < f < 0.6f_{ce}$
$0.4f_{ce} < f < 0.5f_{ce}$
$0.3f_{ce} < f < 0.4f_{ce}$
$0.2f_{ce} < f < 0.3f_{ce}$
$0.1f_{ce} < f < 0.2f_{ce}$
$f_{LHR} < f < 0.1f_{ce}$
Mlat
MLT
0
12
24
10
20
1.0
0.8
0.6
0.4
0.2
0.0
Occurrence rate
of P>noise floor

Figure 3.

Occurrence
Median log10 Power
IQR of log10 Power
Average incl. zero power
(a)
(b)
(c)
(d)
(e)
(f)
(g)
(h)
(i)
(j)
(k)
(l)
f_{ce}
$0.5f_{ce}$
$0.1f_{ce}$
f_{LHR}
0
12
24
MLT
0.0 0.2 0.4 0.6 0.8 1.0
Occurrence rate
−2 −1 0 1 2
$\log_{10}(P)$, pT^2
0.0 0.5 1.0 1.5 2.0
IQR($log_{10}(P)$)
−2 −1 0 1 2
$\log_{10}(P)$, pT^2

Figure 4.

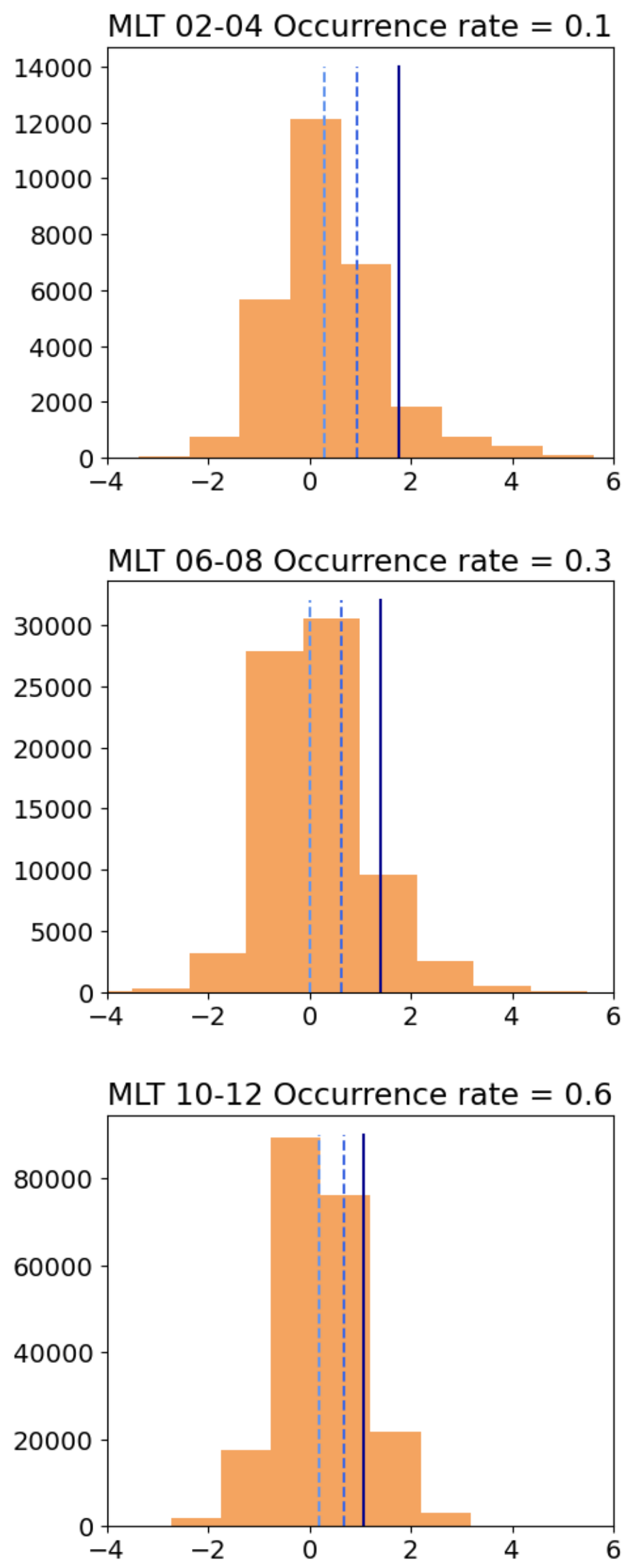
MLT 02-04 Occurrence rate = 0.1
14000
12000
10000
8000
6000
4000
2000
0
−4
−2
0
2
4
6
MLT 06-08 Occurrence rate = 0.3
30000
25000
20000
15000
10000
5000
0
−4
−2
0
2
4
6
MLT 10-12 Occurrence rate = 0.6
80000
60000
40000
20000
0
−4
−2
0
2
4
6
MLT 14-16 Occurrence rate = 0.6
50000
40000
30000
20000
10000
0
−4
−2
0
2
4
6
log10 [P(0.1<f/fce<0.2)], pT2

Figure 5.

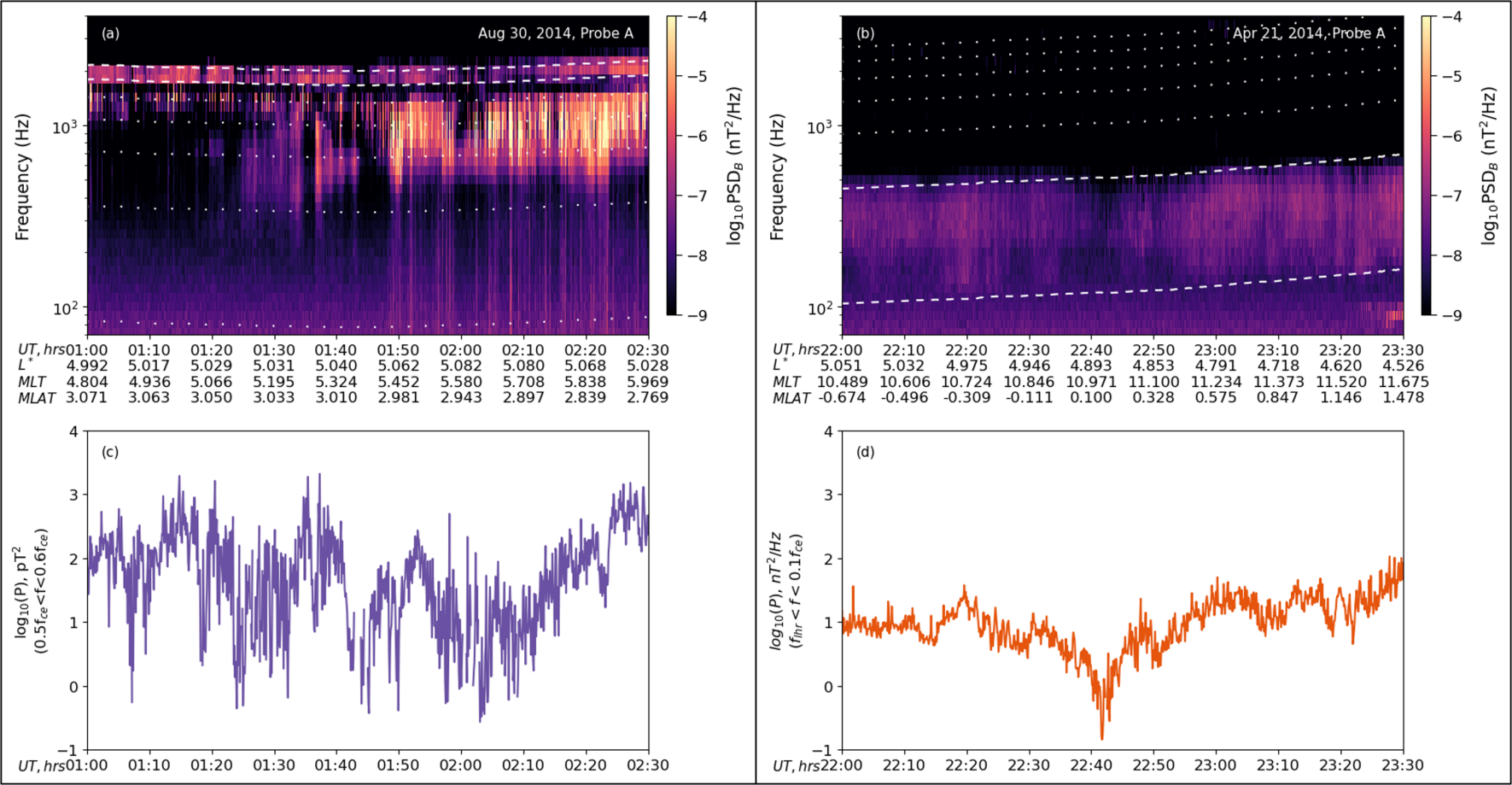
(a)
Aug 30, 2014, Probe A
Frequency (Hz)
10^3
10^2
$\log_{10}PSD_B$ (nT^2/Hz)
−4
−5
−6
−7
−8
−9
UT, hrs 01:00 01:10 01:20 01:30 01:40 01:50 02:00 02:10 02:20 02:30
L^* 4.992 5.017 5.029 5.031 5.040 5.062 5.082 5.080 5.068 5.028
MLT 4.804 4.936 5.066 5.195 5.324 5.452 5.580 5.708 5.838 5.969
MLAT 3.071 3.063 3.050 3.033 3.010 2.981 2.943 2.897 2.839 2.769
(b)
Apr 21, 2014, Probe A
Frequency (Hz)
10^3
10^2
$\log_{10}PSD_B$ (nT^2/Hz)
−4
−5
−6
−7
−8
−9
UT, hrs 22:00 22:10 22:20 22:30 22:40 22:50 23:00 23:10 23:20 23:30
L^* 5.051 5.032 4.975 4.946 4.893 4.853 4.791 4.718 4.620 4.526
MLT 10.489 10.606 10.724 10.846 10.971 11.100 11.234 11.373 11.520 11.675
MLAT -0.674 -0.496 -0.309 -0.111 0.100 0.328 0.575 0.847 1.146 1.478
(c)
$\log_{10}(P)$, pT^2
($0.5f_{ce}<f<0.6f_{ce}$)
4
3
2
1
0
−1
UT, hrs 01:00 01:10 01:20 01:30 01:40 01:50 02:00 02:10 02:20 02:30
(d)
$\log_{10}(P)$, nT^2/Hz
($f_{lhr} < f < 0.1f_{ce}$)
4
3
2
1
0
−1
UT, hrs 22:00 22:10 22:20 22:30 22:40 22:50 23:00 23:10 23:20 23:30

Figure 6.

(a)

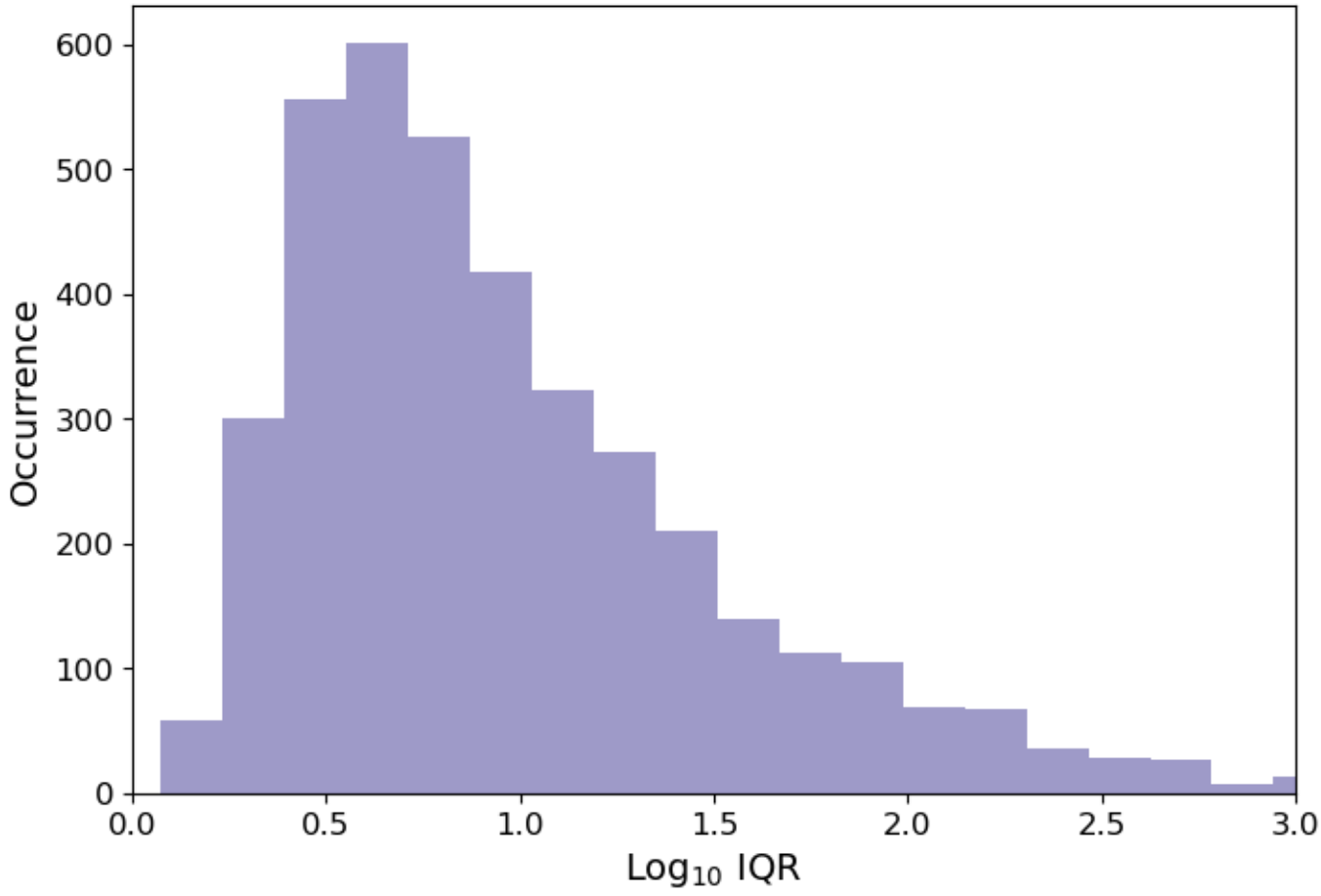
Occurrence
0
100
200
300
400
500
600
0.0
0.5
1.0
1.5
2.0
2.5
3.0
Log10 IQR

(b)

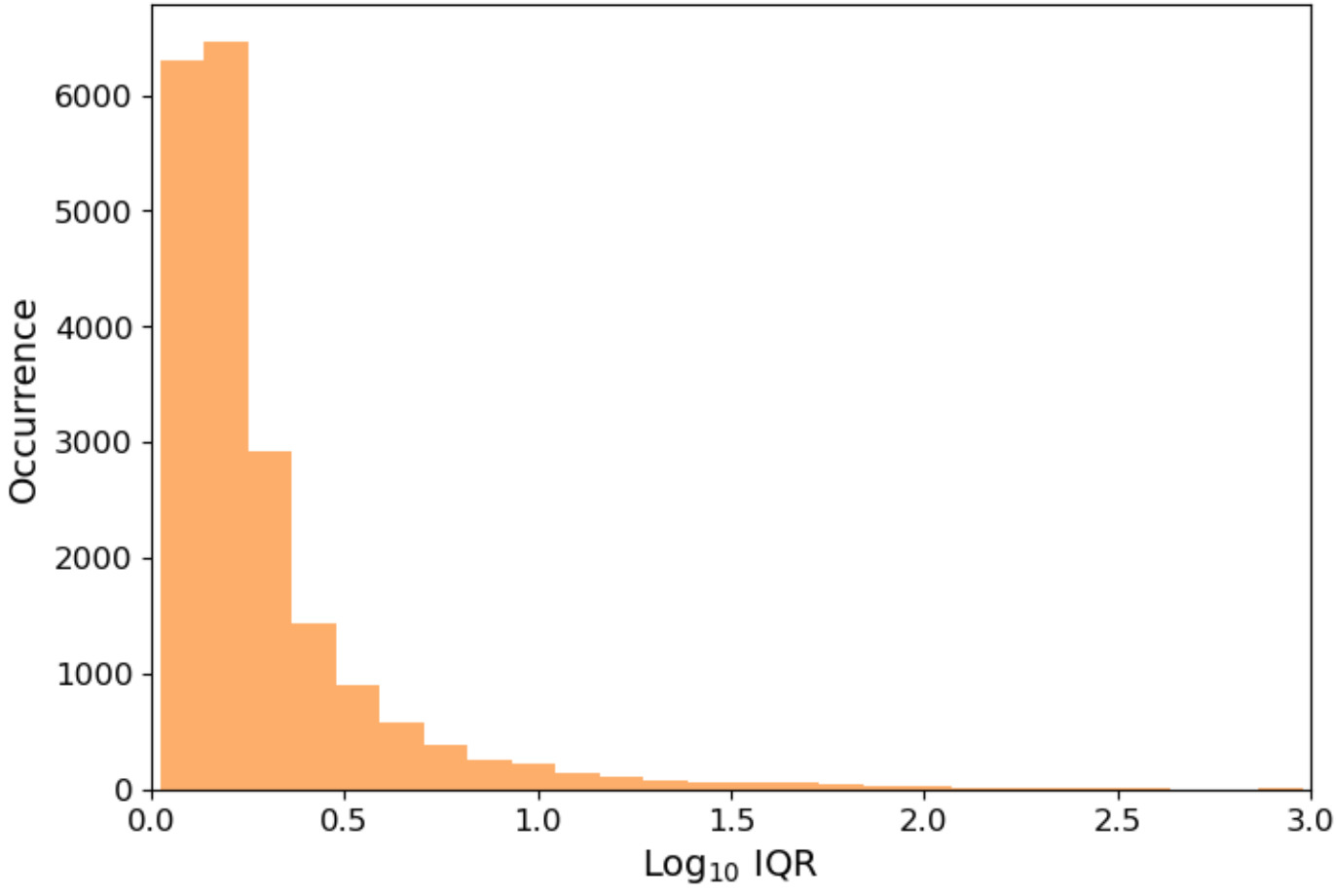
Occurrence
0
1000
2000
3000
4000
5000
6000
0.0
0.5
1.0
1.5
2.0
2.5
3.0
Log10 IQR

Figure 7.

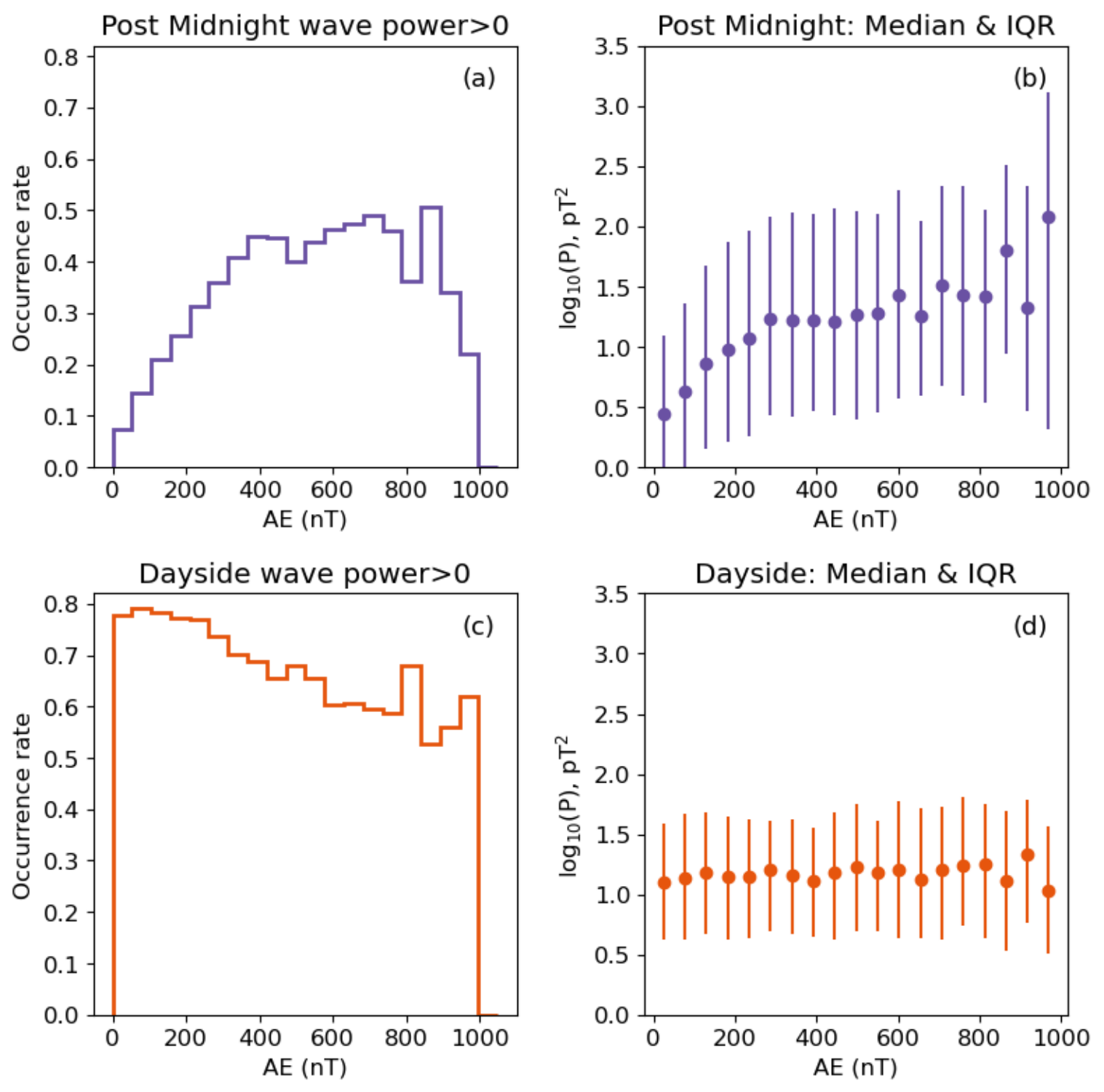
Post Midnight wave power>0
(a)
Occurrence rate
AE (nT)
Post Midnight: Median & IQR
(b)
log10(P), pT2
AE (nT)
Dayside wave power>0
(c)
Occurrence rate
AE (nT)
Dayside: Median & IQR
(d)
log10(P), pT2
AE (nT)

Figure 8.

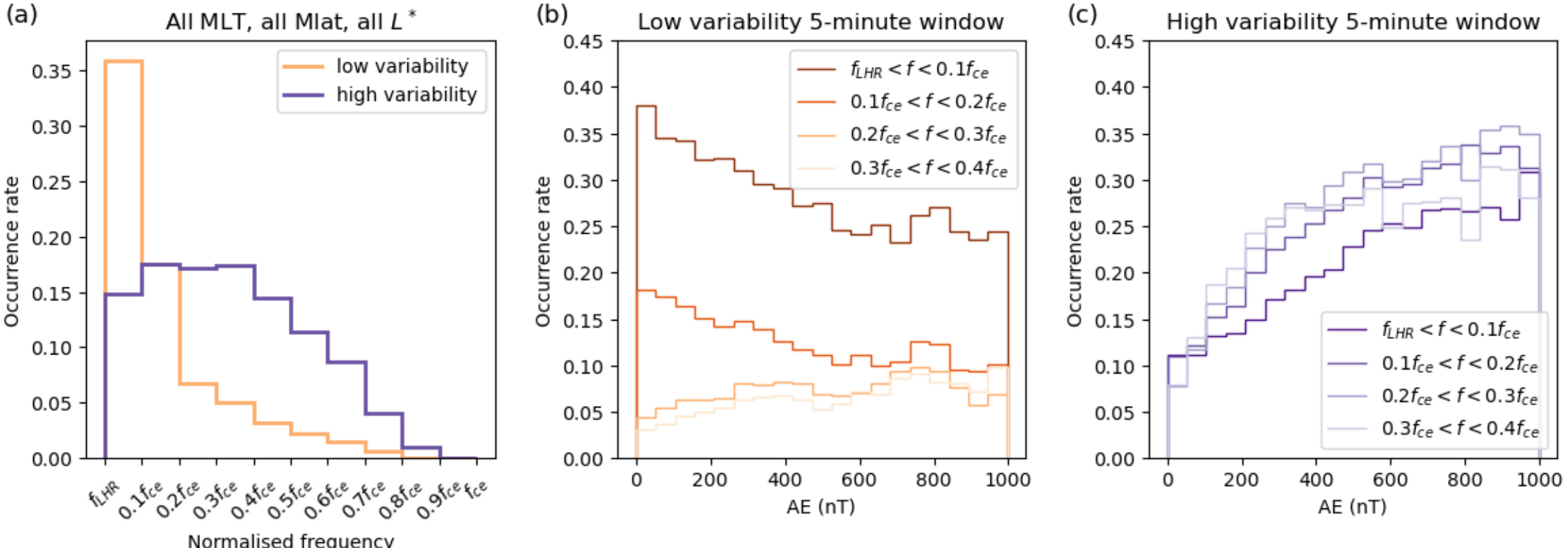
(a)
All MLT, all Mlat, all L^*
low variability
high variability
Occurrence rate
0.00
0.05
0.10
0.15
0.20
0.25
0.30
0.35
f_{LHR}
$0.1f_{ce}$
$0.2f_{ce}$
$0.3f_{ce}$
$0.4f_{ce}$
$0.5f_{ce}$
$0.6f_{ce}$
$0.7f_{ce}$
$0.8f_{ce}$
$0.9f_{ce}$
f_{ce}
Normalised frequency
(b)
Low variability 5-minute window
$f_{LHR} < f < 0.1f_{ce}$
$0.1f_{ce} < f < 0.2f_{ce}$
$0.2f_{ce} < f < 0.3f_{ce}$
$0.3f_{ce} < f < 0.4f_{ce}$
Occurrence rate
0.00
0.05
0.10
0.15
0.20
0.25
0.30
0.35
0.40
0.45
0
200
400
600
800
1000
AE (nT)
(c)
High variability 5-minute window
$f_{LHR} < f < 0.1f_{ce}$
$0.1f_{ce} < f < 0.2f_{ce}$
$0.2f_{ce} < f < 0.3f_{ce}$
$0.3f_{ce} < f < 0.4f_{ce}$
Occurrence rate
0.00
0.05
0.10
0.15
0.20
0.25
0.30
0.35
0.40
0.45
0
200
400
600
800
1000
AE (nT)

Figure 9.

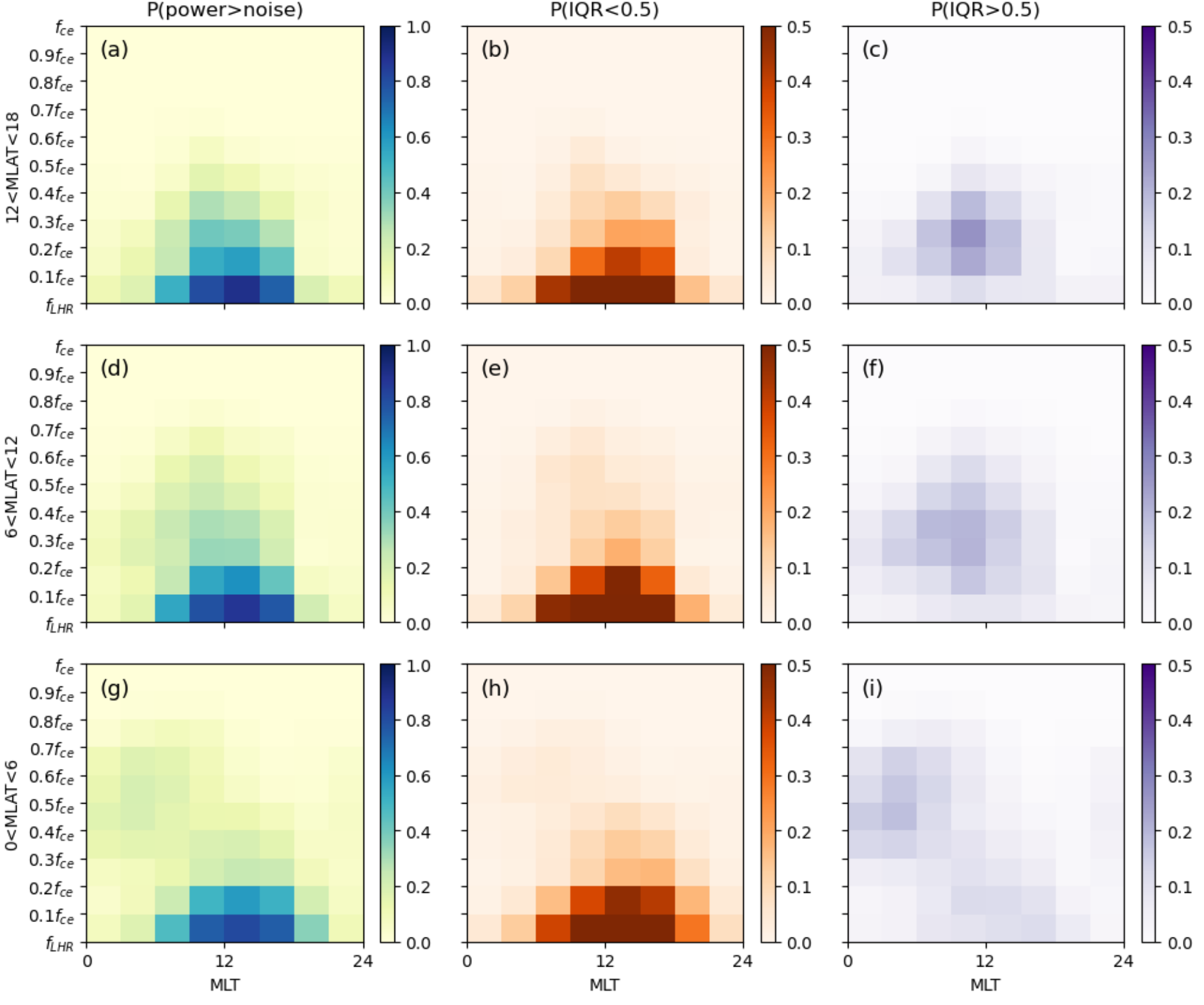
P(power>noise)
P(IQR<0.5)
P(IQR>0.5)
(a)
(b)
(c)
(d)
(e)
(f)
(g)
(h)
(i)
12<MLAT<18
6<MLAT<12
0<MLAT<6
f_{ce}
$0.9f_{ce}$
$0.8f_{ce}$
$0.7f_{ce}$
$0.6f_{ce}$
$0.5f_{ce}$
$0.4f_{ce}$
$0.3f_{ce}$
$0.2f_{ce}$
$0.1f_{ce}$
f_{LHR}
0
12
24
MLT
0.0
0.2
0.4
0.6
0.8
1.0
0.1
0.3
0.5